JGR Solid Earth

RESEARCH ARTICLE
10.1029/2025JB031133

Back to the Source: Connecting the Seismological Observations of Le Teil Earthquake (M_w 4.9, 2019/11/11, France) to the Local Geology

Maxime Godano[1], Christophe Larroque[1,2], Bertrand Delouis[1], Jean-Paul Ampuero[1], Feyza Arzu[1], Françoise Courboulex[1], Anne Deschamps[1], Martijn van den Ende[1], Stéphane Baize[3], and Jean-François Ritz[4]

[1]Université Côte d'Azur, Observatoire de la Côte d'Azur, CNRS, IRD, Géoazur, Sophia Antipolis, Nice, France, [2]Université de Reims Champagne-Ardenne, GEGENA UR3795, Reims, France, [3]ASNR, Autorité de Sureté Nucléaire et Radioprotection, Fontenay-aux-Roses, France, [4]Géosciences Montpellier, Univ. Montpellier, CNRS, Univ. Antilles, Montpellier, France

Abstract The spatial distribution of seismicity in active fault zones depends primarily on the geometry of the fault networks. However, recent advances suggest that seismic activity may also be controlled by the rheology of the geological units surrounding fault zones. In the present work, we use seismological and geological analyses to investigate the influence of the local geology on the rupture nucleation and propagation of the 2019 Le Teil earthquake (France; $M_L = 5.4$; $M_w = 4.9$) and on the distribution of its aftershocks. The kinematic rupture model of the mainshock, obtained by joint inversion of seismological and INSAR data, shows that the rupture nucleated at 1 km depth and propagated mainly up-dip and bilaterally. Template matching detection identifies 115 aftershocks ($-1.6 \leq M_L \leq 2.5$) in the two months following the mainshock. Double difference location shows that the aftershocks delineate a 4 km-long NE-SW plane with a 60° dip to the SE, consistent with the extent and the geometry of the La Rouvière fault activated during the mainshock. By placing the seismicity in the local geological context, we conclude that the seismic activity was largely controlled by the rheological properties of the contrasting lithology. The mainshock nucleated in marly-limestone, but the coseismic slip was maximum above 0.6 km depth in a massive limestone more prompt to store elastic strain. The aftershocks occurred mainly in marls and marly limestone. They are interpreted as ruptures in competent beds of limestones of varying thickness, interbedded with marls.

Plain Language Summary The distribution of earthquakes along active faults depends on the geometry of the faults and the type and strength of the surrounding rocks. In the present work, we investigate through seismological and geological analyses, how an emblematic magnitude 5 earthquake and its aftershocks sequence, recorded in France in 2019, were controlled by the types of rocks in which they occurred. The Le Teil earthquake nucleated at 1 km depth and its rupture propagated mainly bilaterally and toward the ground surface. In the two following months, 115 aftershocks were identified. They are distributed mainly along a plane consistent with the La Rouvière fault which ruptured during the mainshock. The location of the earthquakes in relation to the different geological layers at depth shows that the seismicity is controlled by the type of rock. The Le Teil earthquake nucleated in medium-strength rocks (marly-limestone) with a small amount of slip. It then propagated upward in high-strength rocks (massive limestone) which are capable of producing large slip when they rupture. The aftershocks occur in thin layers of strong limestone, capable of accumulating elastic deformation, interbedded into thick layers of weak materials (marls), which do not have enough strength to nucleate earthquakes.

Key Points:

- Template matching illuminates the aftershock alignment on the 2019 Le Teil earthquake rupture
- Lithology of the sedimentary cover controls both the mainshock rupture propagation and slip distribution, and the location of aftershocks
- Focal mechanisms of the sequence show that the fault was well-oriented with respect to the compressional axis

Supporting Information:

Supporting Information may be found in the online version of this article.

Correspondence to:

M. Godano,
godano@geoazur.unice.fr

Citation:

Godano, M., Larroque, C., Delouis, B., Ampuero, J.-P., Arzu, F., Courboulex, F., et al. (2025). Back to the source: Connecting the seismological observations of Le Teil earthquake (M_w 4.9, 2019/11/11, France) to the local geology. *Journal of Geophysical Research: Solid Earth*, *130*, e2025JB031133. https://doi.org/10.1029/2025JB031133

Received 9 JAN 2025
Accepted 11 AUG 2025

Author Contributions:

Conceptualization: Maxime Godano, Christophe Larroque
Investigation: Maxime Godano, Christophe Larroque, Bertrand Delouis, Jean-Paul Ampuero, Feyza Arzu
Methodology: Maxime Godano, Christophe Larroque, Bertrand Delouis, Jean-Paul Ampuero, Feyza Arzu
Validation: Maxime Godano, Christophe Larroque, Bertrand Delouis, Jean-Paul Ampuero, Feyza Arzu
Writing – original draft: Maxime Godano, Christophe Larroque, Bertrand Delouis

1. Introduction

Active fault zones are complex geological structures of the Earth crust. They host multiple seismic and aseismic processes that accommodate a significant part of the crustal strain. During the interseismic phase, a fault is locked and accumulates shear stress until strength is overcome. Stress is released by earthquake fault slip, which in turn triggers aftershocks at the rupture perimeter or on adjacent faults (e.g., Das & Henry, 2003; Neo et al., 2020; Yamada et al., 2019; Yukutake & Iio, 2017). Seismicity can also comprise earthquake swarms, resulting from transient forcings such as aseismic slip on fault segments surrounding seismic asperities (e.g., Bocchini et al., 2022; Canitano et al., 2021; Martínez-Garzón et al., 2021), fluid pressure (e.g., Baques et al., 2023; Ross

Writing – review & editing:
Maxime Godano, Christophe Larroque, Bertrand Delouis, Jean-Paul Ampuero, Feyza Arzu, Françoise Courboulex, Anne Deschamps, Martijn van den Ende, Stéphane Baize, Jean-François Ritz

& Cochran, 2021) or a combination of both (e.g., De Barros et al., 2020; Jacquemond et al., 2024; Sirorattanakul et al., 2022; Yukutake et al., 2022).

While the distribution of seismicity undoubtedly depends on the geometry of the fault networks, it might also be influenced by the nature of the surrounding geological units and their rheological properties. Progress in earthquake location techniques over the last 25 years allowed to highlight the complex 3D architecture of seismogenic structures in active fault zones (e.g., De Barros et al., 2019; Shelly, 2020; Truttmann et al., 2023; Valoroso et al., 2013). At large scale, Turrini et al. (2015) suggest that both litho-stratigraphy and fault patterns most likely control earthquake distribution in the Po Valley basin. In central Italy, for recent seismic sequences (Colfiorito, L'Aquila, Amatrice-Norcia-Campotosto), Sebastiani et al. (2019) correlate a duality in spatio-temporal patterns of aftershocks with their location in two areas of different lithological and hydrogeological properties. At a smaller scale, for the 2016–2017 Amatrice-Norcia-Campotosto sequence, Carminati et al. (2020) highlight that surface rupture occurred in competent thick carbonate layers, whereas blind-faulting occurred in ductile lithologies (marls and clays) more prone to folding. For the same sequence, Barchi et al. (2021) propose that earthquake distribution is primarily controlled by the litho-mechanical stratigraphy. They show that the seismicity is mostly located in the more competent lithologies that act as a "channel" for the lateral propagation of seismic ruptures on adjacent faults. Collettini et al. (2022) also show in the 2016–2017 sequence, that seismicity localizes not only on the main faults hosting the mainshocks, but also within the surrounding volume. They relate this distributed seismicity to evaporites composed of alternated competent and incompetent layers and proposed that fluid overpressure and shear strain-rate increase during the sequence promote ductile deformation and seismic ruptures within incompetent and competent rocks, respectively.

In this article, we raise the question of the influence of the local geology on seismic sequences, and particularly how it can control the coseismic rupture of a mainshock and the spatio-temporal distribution of its aftershocks. This topic is addressed by a detailed seismological and geological analysis of Le Teil earthquake sequence that occurred on 11 November 2019 in the southeast of France (Figure 1).

The Le Teil earthquake took place in a typical intraplate setting characterized by a very low deformation rate and a low instrumental seismicity (Larroque et al., 2021; Masson et al., 2019). Although of moderate magnitude (M_L 5.4), the ground shaking was surprisingly very strong (modeling of the ground motions suggest that some areas suffered vertical acceleration higher than gravity; Causse et al., 2021) and produced important damage in an area with critical facilities, such as two nuclear power plants, hydroelectric dams on the Rhône River and large quarries. This event has therefore boosted interest in the assessment of seismic hazard in areas of moderate seismicity, although the origin of intraplate seismicity remains under discussion (e.g., Baize & Ritz, 2022; Calais et al., 2016; Ritz et al., 2020). In the day following the earthquake, a rapid response of the scientific community allowed the deployment of 40 seismic stations, InSAR analyses and field surveys (Cornou et al., 2021). Several aspects of the 2019 Le Teil earthquake have already been studied and the main results are the following:

- the focal depth is between 1 and 2 km, the focal mechanism indicates pure reverse faulting, and the moment magnitude is M_w 4.9 (Delouis et al., 2021; Vallage et al., 2021);
- the maximum macroseismic intensity reached VIII EMS98 in the villages of Le Teil, Viviers, and St Thomé, highlighting site effects related to topography and sedimentary filling (Cornou et al., 2021). Based on ground motion modeling, Causse et al. (2021) proposed that several areas suffered an exceptional level of ground acceleration exceeding 1 g;
- despite the dense post-seismic network, only 30 aftershocks were detected in the 3 months following the mainshock using conventional procedures (Cornou et al., 2021);
- InSAR analyses display a sharp rupture striking NE-SW with a relative vertical movement of the two blocks of about 20 cm and an uplift of the SE compartment on a fault plane dipping SE, consistent with the focal mechanism; the maximum coseismic slip is heterogeneously distributed with two patches of 30 cm maximum (Cornou et al., 2021; De Novellis et al., 2020; Marconato et al., 2022; Ritz et al., 2020);
- an almost continuous ground rupture developed at the surface over a length of 4.5 km, southwestward of Le Teil, with vertical offsets in the range of 3–15 cm. These observations are consistent with the InSAR analyses and attest to the reactivation and the inversion of the long-term La Rouvière normal-fault (Marconato et al., 2022; Ritz et al., 2020);
- the natural versus anthropogenic triggering of this earthquake is still a subject of debate and ongoing research (Ampuero et al., 2020; Burnol et al., 2023; De Novellis et al., 2020; Liang & Ampuero, 2020).

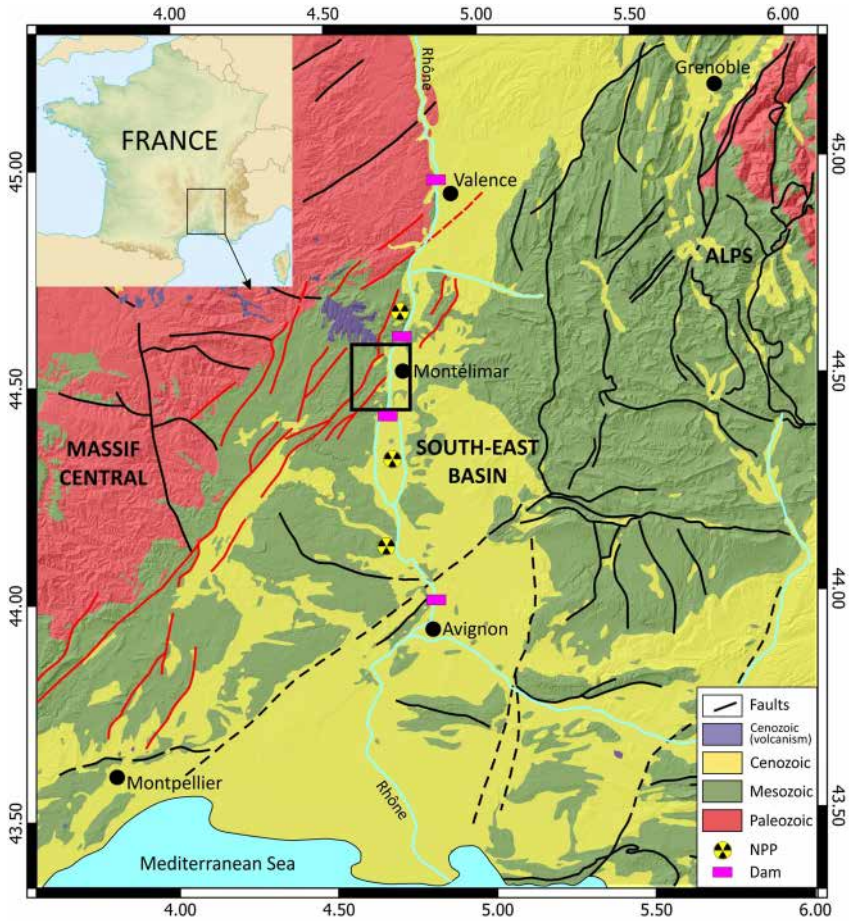

Figure 1. Simplified geological map of the South-East basin of France area (modified from Chantraine et al. (2003)). Paleozoic are mainly crystalline rocks. Mesozoic and Cenozoic are mainly sedimentary rocks (except cenozoic volcanism). Main fault traces are indicated by black lines (solid lines: outcropping faults; dotted lines: hidden faults) and in red the Cévennes faults system (CFS). NPP: nuclear power plant. The black square is the Le Teil earthquake epicentral area (see Figure 2 for details).

For multiple reasons, the Le Teil earthquake is a relevant event to explore links between seismicity and geology. First, the seismic sequence is very shallow (less than 2 km depth). Second, the local geology is well known down to 2 km depth since (a) outcrops of geological units representative of those at the hypocentral depth are accessible in the immediate vicinity of the epicentral area and (b) the lithostratigraphy and geometry of the geological layers are known from 2 deep boreholes and seismic profiles. Third, the post-seismic effort provides an exceptional seismological data set for such a moderate earthquake.

In this study we propose (a) to precisely image the distribution of the co-seismic slip by a seismological/geodetic (InSAR) joint inversion of the mainshock, (b) to complete the aftershock catalog by template matching, relocate most of the aftershocks and determine their focal mechanisms, (c) to discuss the nucleation and propagation of the mainshock and aftershocks ruptures according to the geology and rheology of the faulted area and (d) to discuss the geometrical and stress conditions for inversion of the rupture on the La Rouvière fault.

2. Seismotectonic Setting

The rate of instrumental seismicity is low in the Le Teil area: only 39 earthquakes have been recorded within 20 km of the epicenter between 1962 and 2022 (Figure 2). Their local magnitudes are lower than 2.9 and their focal depths are estimated between 5 and 24 km, with large uncertainties since the nearest station is located 30 km away. Although the seismicity appears diffuse, 20 km southward, in the Tricastin area, a notable shallow swarm occurred in 2002–2003 over several months with some focal depths shallower than 0.5 km (Bollinger et al., 2021;

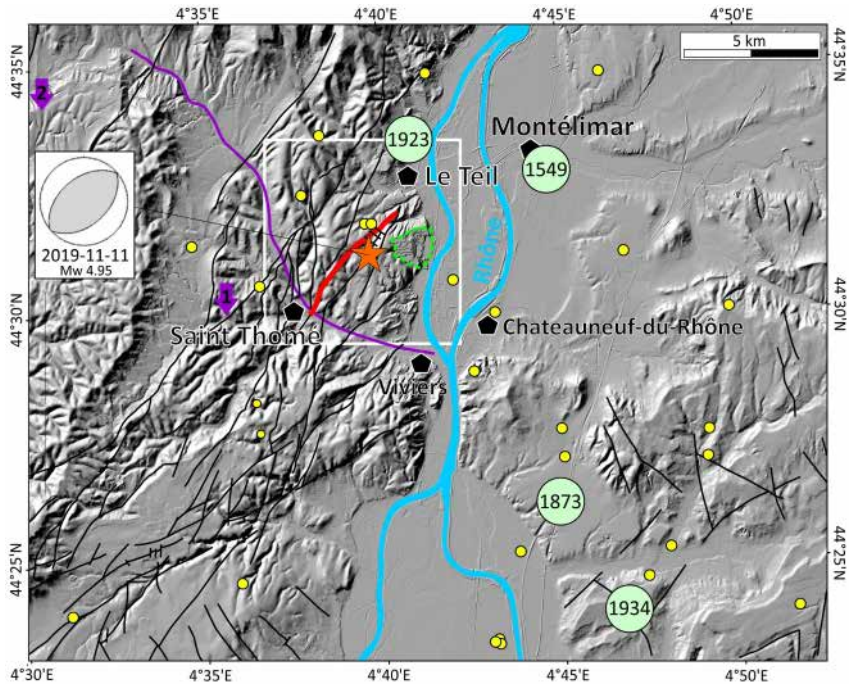

Figure 2. Seismotectonic map of the Le Teil area. Red line: La Rouvière fault. Orange star: epicenter of the 2019 November 11 Le Teil earthquake (44.521°N-4.667°E). Yellow dots: instrumental seismicity 1962–2022 (BCSF-Rénass, 2022). Green circles: historical seismicity (epicentral intensity: 1549-Io VI, 1604-Io V, 1873-Io VII, 1923-Io IV, 1934-Io VII; Jomard et al., 2021). Green dotted line: perimeter of the quarry mentioned in the text. Purple line: EDF seismic profile. Black pentagon: city. Down-pointing purple arrows: Valvignières (1) and Villeneuve de Berg (2) boreholes (scientific cored boreholes). The focal mechanism is from Delouis et al. (2021) (strike 48, dip 45, rake 88). The white square is the area shown in Figure 8a. Black lines: fault traces from the geological map (BRGM). The shaded DTM is from the BD ALTI 25 m (IGN).

Thouvenot et al., 2009). In any case, before 2019, no active fault had been highlighted in the area by the distribution of instrumental seismicity.

Historical archives attest to several seismic events (single events or swarms) mainly located 10–20 km in the Rhône Valley, with macroseismic intensities up to MSK VIII. They occurred in May 1549, January 1610, January–April 1773, July–August 1873 and May 1934, for instance. The largest of these events presumably occurred 8 km south of Le Teil on 8 August 1873, at the end of a 4 months long seismic swarm, and its equivalent moment magnitude was estimated at Mw 4.1 with a focal depth of ∼3 km (Manchuel et al., 2018; Ritz et al., 2020). In the close area surrounding the 2019 earthquake epicenter, events with macroseismic intensity up to V have also been reported in the locality of Viviers in December 1604 and May 1782 and in Le Teil in November 1923.

GNSS data acquired over the last 20 years show horizontal velocities that are too small to accurately measure the slip-rate on the mapped faults. Nevertheless, at regional scale Masson et al. (2019) computed a horizontal strain rate indicating WNW-ESE shortening in the range of $1–2{\cdot}10^{-9}$ yr^{-1}. This shortening direction is consistent with borehole breakout measurements, 35 km north of the epicentral area (site 00609 on the World Stress Map; Heidbach et al., 2018) and indicates a present-day compressive tectonic regime with a very low strain rate.

The Le Teil earthquake resulted from the reactivation of part of the so-called La Rouvière fault (Marconato et al., 2022; Ritz et al., 2020; Vallage et al., 2021). The fault is more than 10 km long and extends further Northeast below the Rhône valley alluvium deposits. It belongs to the NE-SW 120-km-long Cévennes fault system (CFS, Figure 1) that currently separates the Massif Central (a Paleozoic basement domain) from the South-East basin of France (a Meso-Cenozoic sedimentary domain). The CFS is a major structural boundary extensively studied in the field and by seismic reflection profiles, gravity modeling and borehole observations (e.g., Bonijoly et al., 1996; Roure et al., 1992; Roure et al., 1994). Its Mesozoic and Cenozoic evolution display several episodes of mainly strike-slip and extensional faulting. NNE-SSW trending folds near Le Teil and Viviers

are attributed to late Miocene-Pliocene compressive deformation developed from the Western Alpine front (Blès & Gros, 1991; Ford & Lickorish, 2004; Roure et al., 1994). This late compressive deformation does not appear to have inverted the CFS.

This long and complex history led to a structural pattern with ∼100-km-long inherited faults, trending NE-SW and dipping to the southeast (Figure 1). These faults display listric geometries at depth, with high-angle shallow segments (down to 2–3 km depth; Roure et al., 1992; Bonijoly et al., 1996; Thomasset et al., 2024).

3. Data

3.1. Seismological Data

Seismological analyses presented in this study are based on data recorded by sensors of different types belonging to several permanent and temporary networks (Figure S1 in Supporting Information S1). At the time of the mainshock occurrence, the area around Le Teil was covered by few seismological stations. Three permanent stations of the French national seismological network (Epos-France, 1995; RESIF, 1995) were operating within an epicentral distance of 50 km: two broadband velocimeters at 30 km (OGDF) and 45 km (BANN) and one accelerometer at 25 km (OGLP). In addition, two broadband velocimeters (A184A and A192B) of the AlpArray project (AlpArray Seismic Network, 2015; Hetényi et al., 2018), one accelerometer (CRU1) of the French electricity company EDF (Électricité de France), three broadband velocimeters (ADHE, BOLL, PAUL) of IRSN (Institute for Radiological Protection and Nuclear Safety) and four strong motion stations (renamed XSN1 to XSN4 in this paper) belonging to the SNCF train company (Société Nationale des Chemins de Fer Français), were operating within a distance of 20 km to the epicenter. Finally, a short period geophone sensor (station CLAU) dedicated to the monitoring of quarry blasts and placed by the quarry owner in a private house, was recording approximately on the trace of the La Rouvière fault.

In the hours and days following the mainshock, a rapid post-seismic campaign involved the installation in the epicentral area of a dense network of seismological stations composed of 8 accelerometers, 13 broadband velocimeters and 28 short-period sensors (Cornou et al., 2021). These stations allowed to locate 30 aftershocks from 11 November 2019 to 11 February 2020 (Cornou et al., 2021). Most of the aftershocks occurred until mid-January. After that, the seismic activity drastically dropped.

3.2. Geodetic Data

A SAR interferogram (InSAR), mapping the co-seismic surface deformation field induced by the earthquake, was produced and made available by the rapid response team, soon after the earthquake (Cornou et al., 2021). It is based on four pairs of Synthetic Aperture Radar (SAR) images acquired both in ascending and descending geometries. Ascending pairs cover the periods 6 to 12 and 1 to 13 November, and the descending pairs correspond to the periods November 11th to 17th and November 6th to 12th. All images were acquired by the Sentinel-1 satellite (Copernicus program of the European Union, operated by the European Space Agency), combined and processed using the NSBAS software (Grandin et al., 2017). InSAR data points included in our source inversions are displayed in Figure S2 in Supporting Information S1.

3.3. Geological Data

The construction of a precise geological-cross section to a depth of 2-km in the epicentral area is enabled by favorable outcrop conditions and extensive previous field works, which have accurately mapped the trace of the La Rouvière and neighboring faults and the various lithologies surrounding it (Elmi et al., 1996; Marconato et al., 2022; Ritz et al., 2020). Furthermore, subsurface data are available (Figure 2) from (a) a seismic profile recently acquired by EDF in the so-called “vallée de l’Escoutay” and crossing the La Rouvière fault (Thomasset et al., 2024) and (b) two deep boreholes: Valvignières (4,636.3 m depth) and Villeneuve de Berg (2758.6 m depth), 6-km west and 15-km northwest of the epicenter, respectively (geological logs BSS002ARSK and BSS002ARWX available on http://infoterre.brgm.fr).

4. Methods

4.1. Mainshock: Determination of Kinematic Rupture Model From the Joint Inversion of InSAR and Seismic Records

4.1.1. Kinematic Model Parameterization

The kinematic slip model is obtained following the nonlinear multiple windows approach of Delouis, Giardini, et al. (2002). The rupture is represented by a rectangular fault segment, striking 47°N, dipping 57° to the South-East, and extending 6 km along strike and 2.5 km along dip. It is subdivided into small dislocation surfaces (subfaults) with 0.5 km length along both strike and dip. Subfaults are represented by dislocation surfaces to model static surface displacements at the InSAR data points on the Earth surface, and by a point source at their center to model seismic waveforms. Regarding the fault model discretization, the choice of a 0.5 km subfault dimension was made as the best compromise after a series of trial-and-error inversions. Finer discretization does not improve the data fitting, and with coarser discretization, we start to observe an increase in the RMS misfit functions. Fault geometry parameters were adjusted after a series of initial inversions in which different azimuths, dips, and dimensions were tested. We allow the rake to vary along the fault by ±25° around the central value of 90° corresponding to a dominant reverse fault motion. The center of the fault plane model is located at 1 km depth and the plane reaches the surface where surface breaks have been observed (Ritz et al., 2020, Figure S2 in Supporting Information S1).

The local source time function associated with each point source is represented as the sum of three isosceles triangular moment rate functions, mutually overlapping, each with a total duration of 0.3 s. Two bounding rupture velocities, called Vrmin and Vrmax, equal to 0.8 and 3.0 km/s respectively, limit the rupture onset times along the fault by enforcing the constraint $Vrmin \leq dist\_subfault/onset\_time \leq Vrmax$. Here we define dist_subfault as the distance between the subfault center and the rupture initiation point (hypocenter). Within the constrained range, the rupture onset times are allowed to vary freely.

Most of the source parameters in the kinematic model were adjusted through trial and error, starting from an initial estimate based on experience from modeling past earthquakes. For instance, the width of the triangular functions defining the local source time function of each point source is adjusted so that the shortest periods present in the observed bandpass-filtered seismograms can be accurately modeled. The number of triangular functions is adjusted to a minimum value such that increasing this number would only increase computing time without significantly improving the data fit. Regarding rupture velocity (Vr), we did not base our approach on the S-wave velocities in the geological layers of the area. Instead, we allowed the data to determine the range of rupture velocities that best fitted them, starting from a relatively wide possible velocity interval. The initial interval was 1.5–4.0 km/s. Since the inversion systematically produced rupture timing close to the lower bound, we reduced the minimum allowed Vr to 0.8 km/s and also lowered the upper bound to 3 km/s. The lower bound, 0.8 km/s, is consistent with the very superficial nature of the rupture. Setting an even lower limit value does not lead to an improvement in the result.

4.1.2. Seismological Data Selection and Processing

In order to best constrain the kinematic properties of the rupture, which is only a few kilometers long, we used in the inversion the nearest seismic stations, whatever the sensor type and origin, provided that the three-component signals are unsaturated. From the permanent French seismological network (Epos-France) we retained the broadband stations OGDF and BANN, and the strong motion station OGLP. We completed the data set with the strong motion station CRU1 from EDF (Électricité de France), the four strong motion stations XSN1 to XSN4 from SNCF and the short period geophone CLAU located on the La Rouvière fault.

Signal processing of the seismological data includes correction of amplitudes by the sensitivity factor, removal of the pre-event mean amplitude, double integration to displacement, and bandpass filtering. The frequency band used is highly variable, depending on the sensor type and noise level, but is within the flat part of the instrument response. Stations from the permanent French network and EDF cover a broad band of frequencies, while the strong motion instruments from the SNCF are relatively short-periods, usable above 0.25 Hz. Station CLAU is even shorter period, usable in the range 1–3 Hz. The high-frequency cutoff used depends on the epicentral distance, signal complexity and possibility to model the waveforms adequately using a simple velocity model. The justifications of the use of different frequency bands for different sensors are given in Text S2 in Supporting

Information S1. The frequency ranges finally selected for each station are listed in Table S1 in Supporting Information S1.

4.1.3. Inversion Method

The inverted parameters are, for each subfault, the rupture onset time, the amplitudes of the triangular source time functions, and the rake angle. The inversion itself is carried out with a simulated annealing algorithm. The cost function to be minimized is a weighted sum of the normalized RMS (root mean square) misfit functions for each data set, plus a seismic moment minimization function and a smoothing function. The weights assigned to the seismic moment minimization and smoothing functions are adjusted so as not to incorporate excess seismic moment for little gain in data fit, and to avoid incorporating a level of detail in the model that is poorly constrained by the data.

Synthetic seismograms are computed by the wavenumber integration method of Bouchon (1981) with the 1D velocity models adapted to each station. The use of different velocity models is justified by the strong contrast in seismic velocities (particularly in the Vp/Vs ratio) between the western and eastern sides of the Le Teil earthquake (Delouis et al., 2021). The Vp/Vs ratio tends to be low in the west (<<1.73) and high in the east (>>1.73, close to 1.9). We are located on the border between the crystalline Massif Central to the west and the sedimentary basin of south-eastern France to the east, with the major alluvial valley of the Rhône River at its boundary, resulting in a very contrasting geology. Velocity models, which were optimized by trial-and-error, are listed in Table S2 in Supporting Information S1. They display strong variations of the Vp/Vs ratio over the area, as evidenced in Delouis et al. (2021). In the particular case of station CLAU, approximately located on the trace of the ruptured fault plane (Figures S1 and S2 in Supporting Information S1), a uniformly low P-wave velocity of 2 km/s is used for the whole crust, assumed to correspond to the damaged fault zone. This low velocity has been found as the velocity optimizing the waveform modeling of that station.

4.1.4. Constraints on the Inversion

The preferred hypocenter found for Le Teil earthquake by Delouis et al. (2021) using the master event technique is located at 44.5188°N, 4.6694°E at a depth of 1.3 km. One of the point sources in the model is located at these same coordinates, but at a depth of 1.5 km due to the constraint related to the geometry of the fault plane and the discretization of the model. We refer to this point as our initial guess hypocenter. Considering that an uncertainty of the order of ±0.5 km is found by Delouis et al. (2021) both on the epicenter location and the hypocentral depth, we explored whether the joint kinematic inversion of the seismological and InSAR data allowed constraining the position of the hypocenter within these limits, considering that the rupture initiation point could be another source point of the model, among the nearest neighbors of the initial guess point. A slightly better data fit was found for the position located just up-dip from the initial guess point, corresponding to the coordinates 44.521°N, 4.667°E and a depth of 1.0 km. This point is selected as the definitive point of rupture initiation (hypocenter) hereafter.

Considering that the InSAR data we use have been sampled conservatively, avoiding points too close to the trace of surface breaks (Figure S2 in Supporting Information S1), we considered the possibility of taking into account the coseismic vertical offsets estimated by Ritz et al. (2020) as an additional constraint in the inversion. To do so, the slip of the source points forming the upper subfault line in the model is constrained to be greater than or equal to the estimated total vertical offset found by these authors. The freedom left to slip to be greater than this value is justified by the existence of a horizontal component of the reverse fault motion. The horizontal offset combines with the vertical one to increase the total slip along the dip of the fault.

The CLAU station being located much closer to the rupture than the other stations (Figure S2 in Supporting Information S1; see also the higher amplitudes of that particular station in Figure S5 in Supporting Information S1), and its sensor being usable on a limited band at high frequency only, we assign it a weight five times smaller than the other stations. We also carried out inversions without this station to check that it alone does not modify strongly the result.

4.2. Aftershocks Analysis

4.2.1. Detection by Template Matching

We use the template matching technique (e.g., Gibbons & Ringdal, 2006) to detect additional small aftershocks that complement the aftershock catalog of Cornou et al. (2021). We focus on the 2 months that follow the mainshock (12 November–20 January), during which the seismicity is the most active. We take as template a selection of 19 earthquakes from the catalog of Cornou et al. (2021), with a local magnitude between −0.3 and 2.5 (Figure S9 in Supporting Information S1). We have limited the template matching to these 19 templates to reduce the computational time. These are aftershocks with the highest magnitudes and have been chosen to be representative of the diversity of the recorded waveforms. Template matching is performed on a selection of 10 of the 28 deployed short-period sensors (N01, N02, N04, N07, N09, N10, N13, N18, N22, N26). The selected sensors display a relatively low microseismic noise and are little affected by transient interfering noises caused by human activity.

We apply a basic method of template matching. Only vertical components of the seismograms are used, to limit the processing time. Data are bandpass-filtered in the 2–20 Hz frequency band. The template data are 5 s long windows including P and S waves. For each station, each template is cross-correlated with daily continuous data, by sliding the window with 1 s of overlap, producing a continuous cross-correlation function sampled at the original sampling rate of each station. For a given station, a detection is defined when the cross-correlation coefficient exceeds a threshold of 0.55. This value may appear low, but a higher threshold of cross-correlation coefficient (0.7, 0.65, or even 0.6) would lead to the non-detection of low magnitude aftershocks. Indeed, due to the ambient noise, and despite the applied bandpass filter, earthquake waveforms are strongly affected by noise. Consequently, cross-correlating templates with low magnitude aftershocks in the continuous signal gives relatively low cross-correlation coefficient. For these reasons, in a first step, we choose to take a low cross-correlation threshold of 0.55 to capture low magnitude aftershocks, even if this also leads to false detections. But the threshold of 0.55 seems to be a good compromise to maximize the number of detected aftershocks while minimizing the number of false detections. In a second step, we carry out careful visual inspection to discard false detections. Once all the 10 stations have been scanned by template matching, we keep the events that have been detected at least at two stations. The magnitude of a new detection (M_L^{detec}) is estimated from the magnitude of the template with which it best correlates (M_L^{temp}) and from the ratio between its maximum amplitude ($A_{\text{max}}^{\text{detec}}$) and the maximum amplitude of the template ($A_{\text{max}}^{\text{temp}}$), as follows:

$$M_L^{\text{detec}} = M_L^{\text{temp}} + \log_{10}\left(A_{\text{max}}^{\text{detec}} / A_{\text{max}}^{\text{temp}}\right) \quad (1)$$

4.2.2. Location Procedure

We first refine the location of the 19 templates by relocating them in a local velocity model with the NonLinLoc software (Lomax et al., 2000). P and S arrival times measured on the 52 stations of the Le Teil postseismic network are inverted. We estimate an average error of 0.05 and 0.1 s for the P and S pickings, respectively. The most likely hypocenter location is provided by the oct-tree importance sampling algorithm implemented in NonLinLoc.

We evaluate the influence of the velocity model on aftershock locations by comparing results based on two different local velocity models constructed thanks to the temporary stations deployed after the mainshock. The first one is that of Delouis et al. (2021) (hereinafter VM1) defined as a 1D linear velocity crustal model (Figure S3 in Supporting Information S1). The second one is that of Causse et al. (2021) (hereinafter VM2) defined between the surface and 6 km depth, as a 1D layered model (Figure S3 in Supporting Information S1). The latter features low velocity layers between 1.2 and 2.2 km depth, consistent with soft Valanginian marls observed in the field and in boreholes at this depth range.

The events detected by template matching are next located with the double-difference relative location method (HypoDD software; Waldhauser & Ellsworth, 2000). We inverted the differential P and S arrival times (a) obtained from the manual pickings of the 19 templates (catalog times, 3528 P and 3582 S) and (b) computed by cross-correlating each earthquake pair of the template matching catalog (cross-correlation times). The cross-correlation analysis was performed on 0.5 s long windows containing P and S waves. A Butterworth

bandpass-filter from 2 to 20 Hz was applied on the waveforms. We kept only cross-correlation times for cross-correlation coefficients ≥0.78, leading to 11,739 P differential times and 17,266 S differential times. This coefficient threshold is a compromise between the quality and the quantity of the measured delay times. Indeed, only strong cross-correlated events are kept, which reduces the measurement error and consequently the location uncertainty. A higher threshold would decrease the number of delay times and consequently the number of located events. The initial location of the new events detected by template matching is set at the location of the template with which they best correlate. For the catalog times, the same weight was applied for P and S times. The cross-correlation times are weighted by their correlation coefficient. The relocation was performed using the least square inversion implemented in HypoDD. In order to assess the influence of the velocity model, the double-difference relocation is also performed in both velocity models VM1 and VM2.

The relative location uncertainties are assessed by a bootstrap method proposed by Waldhauser and Ellsworth (2000). Residual times arising from the final double-difference location are randomly sampled with replacement and used to relocate earthquakes. This process is repeated 200 times. The 95%-distribution of the cumulative relocations gives an estimation of the relative uncertainties in the x, y and z directions.

4.2.3. Focal Mechanisms Determination

Focal mechanisms are computed for the 19 templates ($-0.3 \leq M_L \leq 2.5$) by using the joint non-linear inversion of polarity and amplitude of direct P, Sv, and Sh waves and Sv/P, Sh/P, Sv/Sh amplitude ratios, proposed by Godano et al. (2009, 2014). The dense coverage of the area by the temporary seismic network provides a strong constraint for the focal mechanism computation. Consequently, only P polarity and S/P amplitude ratio are used as input data.

Amplitude (P or S) is defined as the first peak directly after the wave onset (first motion). Practically, amplitude is taken as a Euclidian norm:

$$A = \sqrt{{A_{NS}}^2 + {A_{EW}}^2 + {A_Z}^2} \tag{2}$$

where A_{NS}, A_{EW}, and A_Z are the amplitudes of the first motions manually measured on the E-W, N-S, and vertical components of the seismogram, respectively. Then the S/P ratio is computed.

P polarity is defined as the sign of the P wave first motion on the vertical component (positive sign = compression, negative sign = dilatation). Measurements are performed on Butterworth bandpass-filtered data between 2 and 40 Hz.

The optimal fault plane solution results from a random exploration, operated by a simulated annealing algorithm, over values of strike, dip and rake. The suitability between the observed and theoretical data corresponding to the optimal solution is measured by a score function (Godano et al., 2014).

The uncertainties of the focal mechanisms are assessed by following a stochastic approach. Noise in seismograms and earthquake location uncertainties are sources of uncertainties on fault plane solution. Therefore, after finding the optimal fault plane solution, 50 inversions are performed with randomly perturbed data and location. For each station, the perturbation applied to the amplitude is drawn from a Gaussian distribution with zero mean and the same standard deviation as a noise window. Practically, this standard deviation is computed on the Euclidian norm of 3 noise windows of 1 s length taken on each component of the seismogram directly before the P or S wave. Such approach also allows the possibility to change the P polarity. Coordinates of earthquakes are perturbed with values randomly drawn from Gaussian distributions of zero mean and standard deviation equal to the E-W, N-S and vertical location uncertainty. Finally, the distribution of the 50 "perturbed" solutions gives an estimation of the focal mechanism uncertainties.

5. Results

5.1. Kinematic Rupture Model of the Mainshock

The slip distributions obtained without and with the near-surface slip constraint are presented in Figure 3. The main effect of the constraint is a shift of the maximum slip location near the surface, from positions −1.5 km and

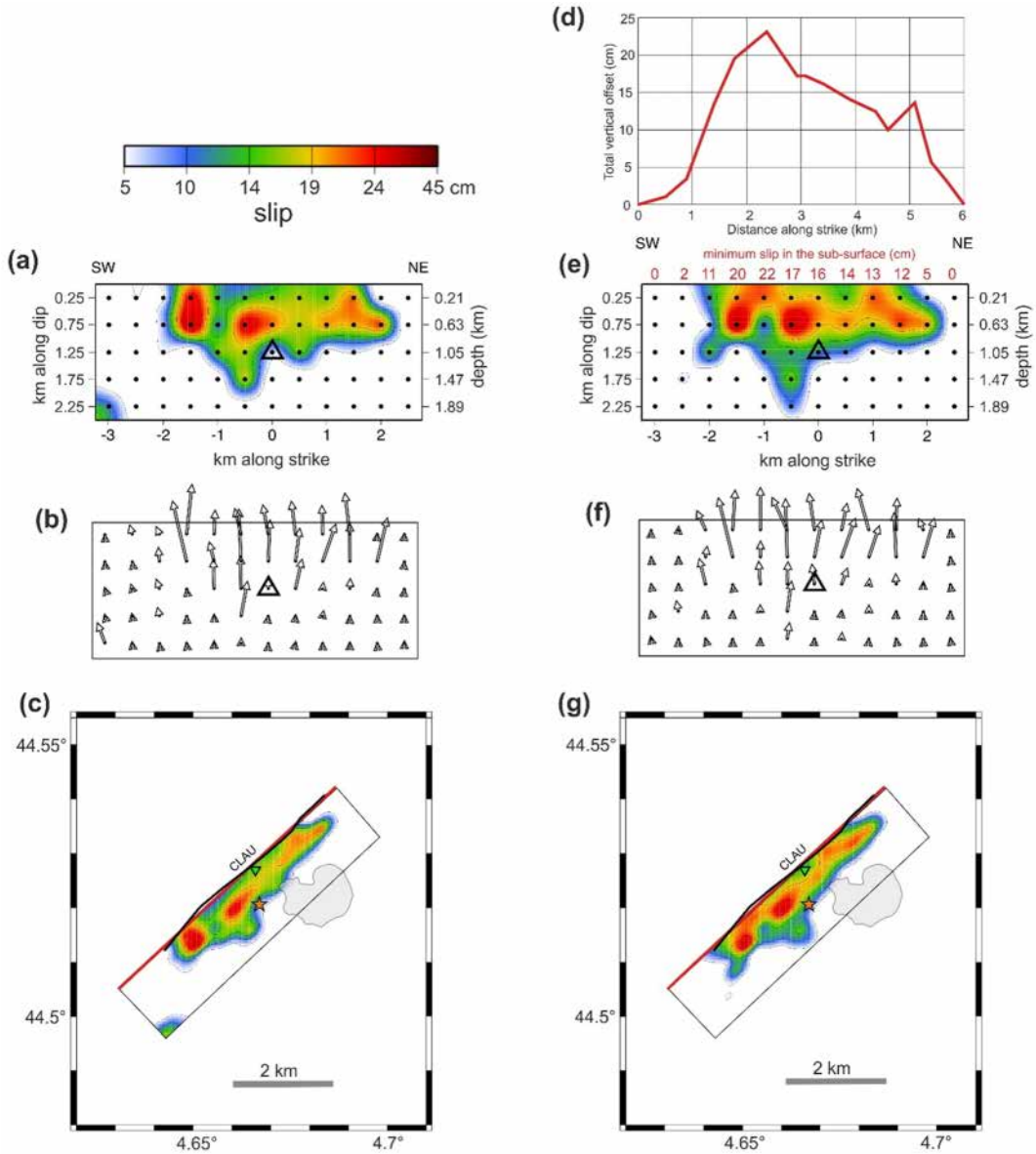

Figure 3. Result of the joint inversion of InSAR and seismological data. Left and right columns show the result without and with an additional constraint on the minimum value of slip in the near-surface, respectively. (a) and (e): Slip distributions along strike and dip. Small black dots: point sources at the center of subfaults. Open triangle: hypocenter. On top of (e), the numbers in red correspond to the total vertical offset estimated from the InSAR data shown in (d), redrawn from Ritz et al. (2020). The slip of the upper line of subfaults in (e) is constrained in the inversion to be greater than or equal to the value (in cm) indicated in red just above them. (b) and (f): Slip vectors showing the motion of the hanging wall (upper block), with size proportional to slip. Open triangle: hypocenter. (c) and (g): Slip distributions projected onto the surface. Red heavy line: top of the fault model at the surface. Black heavy broken line: simplified trace of observed surface breaks, from Ritz et al. (2020). Orange star: epicenter. Light gray shaded area: approximate contour of the limestone (cement) quarry. Green triangle: short period vibration geophone, station CLAU.

+1.5 km along strike without constraint (Figure 3a) to positions −1 and +1 km with constraint (Figure 3e). With the constraint, the normalized RMS misfit increases by 0.8% for the seismological data (negligible) and decreases by 2% for the InSAR data (slightly beneficial). Overall, we consider that this constraint fits well with the data, and the solution with constraint is our preferred solution (right column of Figure 3).

The seismic data alone do not effectively constrain the slip distribution due to trade-offs between the spatial location of slip and rupture timing when the rupture velocity is allowed to vary, which is necessary since it is a

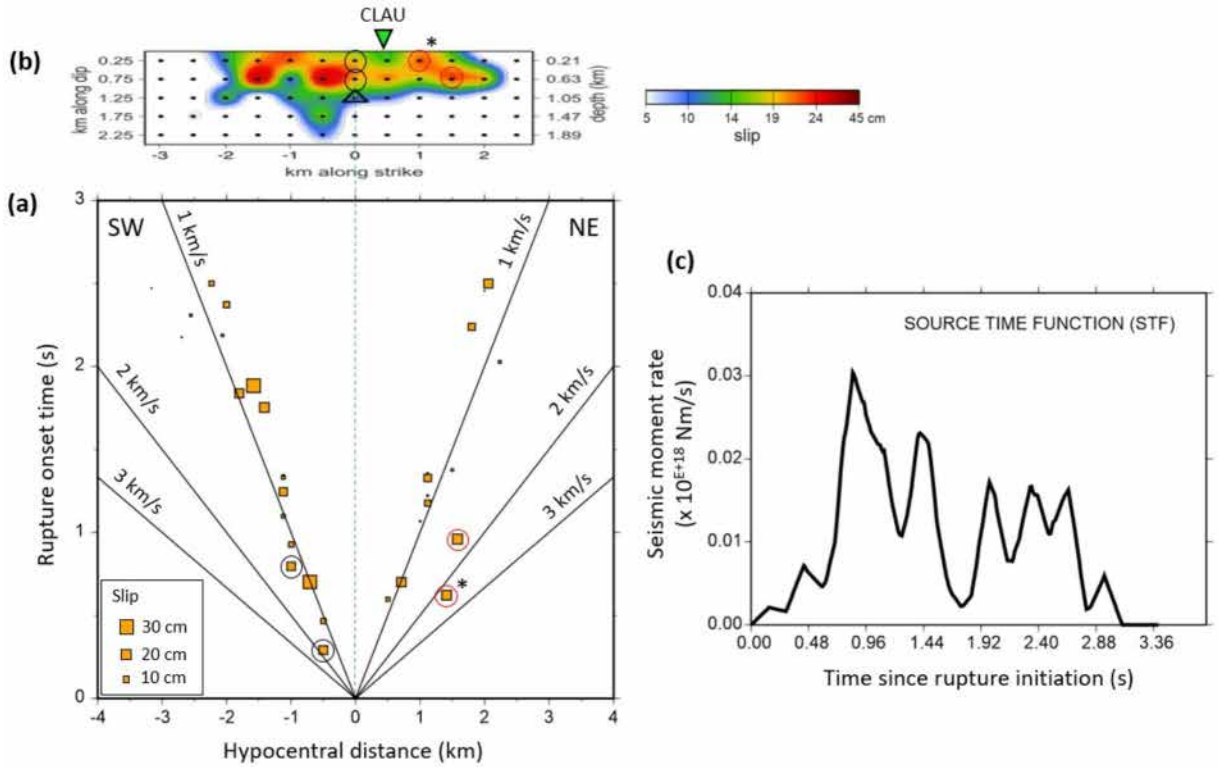

Figure 4. Rupture timing in our preferred finite source inversion model. (a) Time-distance plots of slip. Orange squares: subfault onset time as a function of hypocentral distance, with size proportional to slip, from the joint inversion of the InSAR and seismological data. Oblique black lines: average rupture speeds of 1, 2 and 3 km/s, for reference. The onset time is the time when a subfault begins to slip. The orange squares circled in black correspond to the sub-faults located above the hypocenter (marked also in b), with a rupture propagation which is updip, not toward the SW. The orange squares circled in red correspond to a fast rupture speed toward the NE. The fastest speed ~2.3 km/s (star) is only found when the CLAU station is included in the inversion. (b) Slip distribution along strike and dip (same as in Figure 3e). Black and red circles indicate the center positions of the subfaults marked in the same way in (a). The projection onto the fault trace of the closest seismic sensor CLAU is shown on the top. (c) Overall source time function (STF).

priori unknown. This limitation can be overcome with very dense seismic networks, where several stations are closer than the rupture dimension. However, this is not the case here, as only one station (CLAU) is at such a short distance. By jointly inverting the seismic records with InSAR data, the location of slip is primarily constrained by the InSAR data. This allows the seismic data to provide information about rupture timing (such as rupture duration and velocity) and rupture directivity (whether unilateral, bilateral, etc.).

The resulting rupture length is 4 km and the co-seismic slip is confined above 1.5 km depth, even essentially above 1 km depth (Figure 3). The rupture evolution is a combination of up-dip and bilateral horizontal (to the NE and to the SW) propagations. The average rupture speed is rather slow, 1.1 km/s, possibly due to the shallow depth of the rupture. Without station CLAU, the average rupture speed is 1.0 km/s. The maximum slip amounts to ~30 cm and occurs at a depth of ~0.6 km on two asperities in the SW side of the rupture (Figure 3e). The overall seismic moment, 3.37E+23 dyne.cm, is equivalent to a moment magnitude M_w 4.95.

Toward the SW, the rupture propagates quite regularly and the rupture speed remains close to the average speed of 1.0 km/s (Figure 4a). The rupture timing shows more variation toward the NE. The areas with high values of slip located 1 and 1.5 km NE of the hypocenter (circled in red on Figures 4a and 4b) tend to break ahead of the rest of the rupture. There, the rupture speed reaches 1.6 and 2.3 km/s (Figure 4a). For the point located close to the surface (marked with an asterisk in Figures 4a and 4b) this feature is only present if the CLAU station is included in the inversion. Without this station, the rupture speed of this point remains close to the average value of 1 km/s. In total, the rupture lasts for about 3 s, as shown by the overall source time function (Figure 4c).

We verify that the variations in timing and associated rupture speed are required by the seismological data by performing inversions in which the rupture speed is fixed. As shown in Figure S4 in Supporting Information S1,

the best fixed velocity found is 1 km/s, equal to the average velocity of our preferred inversion, but it leads to a larger misfit for the seismological data than the inversion with variable rupture velocity.

The modeling of the data obtained with our preferred inversion, that is, with the constraint on the subsurface slip and variable rupture speed (Figure 3 right column and Figure 4), is displayed in Figures S5 to S7 in Supporting Information S1. A synthetic test to assess the resolution of the kinematic inversion is detailed in Text S1 and Figure S8 in Supporting Information S1.

5.2. Spatio-Temporal Distribution and Focal Mechanisms of the Aftershocks

5.2.1. Detection of New Aftershocks

The template matching procedure provided 823 detections. Many are false detections resulting from correlation of the P or S wave of a template with noise transients. Hence, we performed a careful visual check to remove such false detections. As a result, 96 detections were identified as earthquakes. Along with the 19 templates, the new catalog contains 115 aftershocks (Figure 5a). The local magnitude ranges from −1.6 to 2.5.

Overall, the rate of aftershocks decreased over the period of 2 months that followed the mainshock. Most of the seismic activity (∼70% of events) occurred in November, with an average rate of 4.3 earthquakes/day and including the two largest aftershocks with $M_L > 2$. In December, the aftershock activity was relatively quiet (average rate of 0.5 earthquakes/day) and the events had $M_L < 1$. Finally, during the first 10 days of January, the activity slightly increased (average rate of 1.3 earthquakes/day) and then stopped after the 13th.

We fit the Omori-Utsu law to the aftershock sequence (Utsu, 1961). This law describes the aftershock rate λ as a function of elapsed time t since the mainshock as

$$\lambda(t) = K(t + c)^{-p} \tag{3}$$

where p (decay exponent), K (productivity) and c (delay time of the power law onset) are constants. Fitting with the maximum log-likelihood method yields $p = 0.95$, $K = 22$, and $c = 1.25$ day. Details of the method are given in Text S3 in Supporting Information S1. Figures 5b and 5c display the fit of the Omori-Utsu law to the aftershock sequence.

The frequency-magnitude distribution of the aftershock sequence is displayed in Figure 5d. We visually estimate a magnitude of completeness (M_c) around −0.5. The Gutenberg-Richter b-value, estimated with the maximum likelihood method (Aki, 1965), is low, $b = 0.62 \pm 0.07$. To assess the stability of this solution, b-value is also computed by considering $M_c = -0.6$ and $M_c = -0.4$. Results give b-values of 0.57 ± 0.06 and 0.63 ± 0.07 respectively, which is close to the b-value obtained with $M_c = -0.5$.

The Omori-Utsu law and b-value parameters will be discussed in Section 6.2.

5.2.2. Location

The absolute location of the 19 templates in VM1 with NonLinLoc is displayed in Figure S9 in Supporting Information S1. Compared to the initial location of Cornou et al. (2021), the epicenters are more clustered and clearly draw a ∼4 km-long NE-SW alignment. At depth, the seismicity is located between 0 and 3 km depth and delineates a plane steeply dipping toward SE. The location uncertainty is on average 60 m horizontally and 160 m vertically, with maximal values of 200 m horizontally and 500 m vertically. The location in VM2 is displayed in Figure S10 in Supporting Information S1. Compared to VM1, epicenters are sparser. In depth, the seismicity is divided in two clusters, one near the surface and the second below 2 km. The location RMS in VM1 is one order of magnitude lower than in VM2 (Figure S11 in Supporting Information S1). Thus, VM1 explains better the measured P and S times and is more suitable for location. These results corroborate the observations of Van den Ende et al. (2024) who showed that VM1 provides a better fit than VM2 to the aftershock data recorded by distributed acoustic sensing along a local fiber optic cable.

The double-difference relative location of the entire aftershock catalog in VM1 is successfully achieved for 84 out of 115 events. The resulting locations confirm an overall ∼4 km-long SW-NE plane with 60° dip toward SE (Figure 6). The seismicity deepens from SW (0.4 km depth) to NE (2 km depth). The seismicity plane features

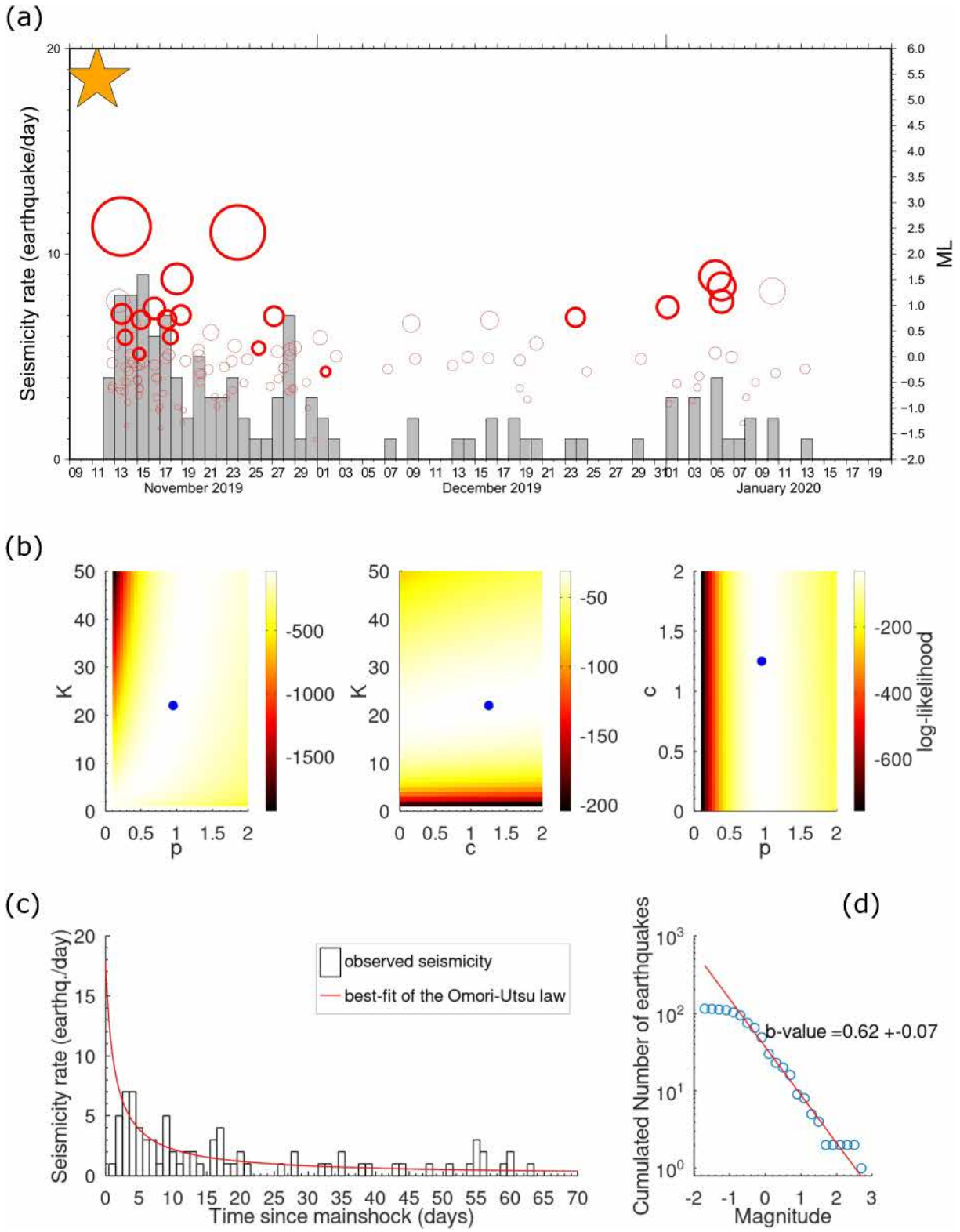
(a)
Seismicity rate (earthquake/day)
ML
November 2019
December 2019
January 2020
(b)
K
p
c
log-likelihood
(c)
observed seismicity
best-fit of the Omori-Utsu law
Seismicity rate (earthq./day)
Time since mainshock (days)
(d)
Cumulated Number of earthquakes
b-value =0.62 +-0.07
Magnitude

Figure 5.

several imbricated clusters. They delineate sub-parallel small lineaments and planes that plunge toward SE with variable dip ranging between 35° and 60°.

For comparison, the double-difference location is also performed in VM2. The 87 successfully relocated events are sparser compared to the locations in VM1 (Figure S12 in Supporting Information S1). In depth, the seismicity ranges between 1 and 3 km and is composed of poorly-defined clusters dipping toward NW and SE. RMS and residual times in the double-difference relocation are clearly lower for location in VM1 than in VM2 (Figure S13 in Supporting Information S1). We conclude that VM1 is more suitable for earthquakes location than VM2. In the following, we will focus on the locations obtained in VM1.

The double-difference location uncertainty is estimated around 10 m horizontally and vertically (Figure S14 in Supporting Information S1). This uncertainty is the relative location error inside the cloud of aftershocks. However, the uncertainty on the absolute position of the cloud might be higher, at most comparable to the average absolute location uncertainty estimated for the 19 templates.

5.2.3. Focal Mechanisms and Stress Tensor

Focal mechanisms are computed by using VM1 and the double-difference locations obtained with VM1. The 52 stations of the Le Teil postseismic network are used, which corresponds to a maximal azimutal gap around 33° and a mean azimuthal gap around 7°. Obviously, depending on the earthquake, polarities and amplitude ratios are not always measurable. Hence the number of used stations and the azimuthal gap can vary from earthquake to another. Fault plane solutions are displayed on map view and on a N135°E cross section in Figure 6. For each earthquake, the used station, their distribution on the focal sphere, the P polarities and S/P amplitude rations are given by the stereodiagram displayed in Figure S15 in Supporting Information S1.

The focal mechanisms have an outstanding homogeneity: they all show reverse faulting, with a minor strike-slip component for a few of them. They globally strike along the NE-SW direction and have a nodal plane dipping around 60° toward SE, compatible with the alignment of the seismicity. These solutions also agree with the focal mechanism of the mainshock (Delouis et al., 2021 and Figure 2).

Uncertainties are assessed by drawing perturbed locations from a Gaussian distribution with standard deviation equal to the maximum uncertainty estimated during the initial step location of the 19 templates (200 m horizontally, 500 m vertically). These values may appear high, but the resulting great variability of station positions on the focal sphere is a mean to mimic variability related to the velocity model uncertainty (not considered in the estimation process of focal mechanism uncertainty).

On average, south-east dipping nodal planes have an uncertainty of 6°, 8°, and 14° on strike, dip and rake, respectively. North-west dipping nodal planes are globally less well constrained, with average uncertainty of 16°, 7°, and 19° on strike, dip and rake, respectively. Given the uncertainty on rake, we conclude that minor strike-slip components in the fault plane solutions are not significant. The focal mechanisms of the 19 aftershocks and of the mainshock (Figure 2) are jointly used to invert for the local stress tensor, following the approach presented in Delouis, Déverchère, et al. (2002). This results (Figure 7) in a predominantly compressional stress regime (shape factor $R < 0$; Rivera & Cisternas, 1990), although the similarity between the focal mechanisms induces large uncertainties in the stress tensor parameters. The best compression axis σ_1 is oriented 127°N and plunges 20° SE (best solution, Figure 7). The best extension axis σ_3 is oriented 277°N and plunges 67°W, while the best intermediate axis σ_2 is oriented 34°N and plunges 10°NE. It should be noted that the result of the focal mechanisms inversion is consistent with the NW-SE compressional stress state derived at the regional scale, on the one hand from GNSS data (Masson et al., 2019) and on the other hand from borehole breakout measurements (Heidbach et al., 2018).

Figure 5. Earthquake statistics. (a) Daily rate of aftershocks (gray histogram) detected in the 2 months following the M_L 5.4 (M_w 4.9) mainshock (orange star). Bold red circles correspond to the 19 templates and thin red circles to the 96 new detections by template matching. (b) Omori-Utsu law of the aftershock sequence: Log-likelihood representation in the space of parameters K, c, and p explored by grid search (Text S3 in Supporting information S1). Blue dot indicates the parameter values corresponding to the maximum log-likelihood. (c) Best fit of the Omori-Utsu law (red curve) to the observed rate of aftershocks (white bars). Best fit is obtained for K, c and p values that maximize log-likelihood. (d) Frequency magnitude distribution of the aftershock sequence (blue dots). The red line is the Gutenberg-Richter relation with a b-value of 0.62 computed with the maximum likelihood method (Aki, 1965).

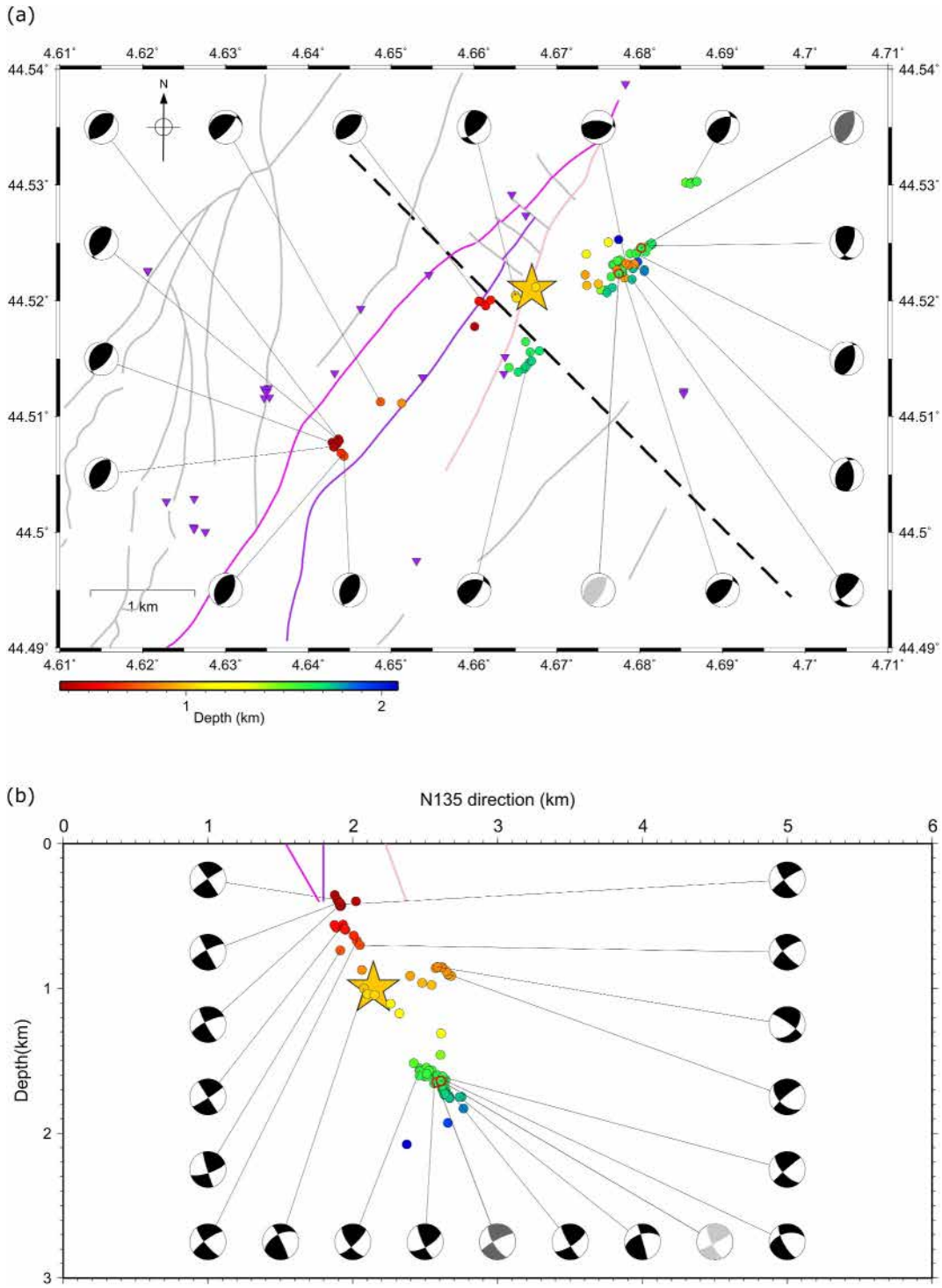

Figure 6. Location of 84 aftershocks located by double-difference in velocity model VM1 (circles colored by depth) and focal mechanisms for 19 of them. (a) Epicenter map. Orange star: mainshock epicenter (Section 4.1.4). The two main aftershocks of M_L 2.5 and M_L 2.4 are marked by red-bordered circles and by dark-gray and light-gray focal mechanisms respectively. Bold lines are faults: La Rouvière fault (magenta), Bayne-Roche Renard fault (purple), Paurière fault (pink), other faults (gray). Purple triangles: seismological stations. Black dashed straight line: 135°N cross section of panel (b). (b) 135°N vertical cross-section. Trace and dip of faults near the surface are indicated by colored segments: La Rouvière fault (magenta), Bayne-Roche Renard fault (purple), Paurière fault (pink).

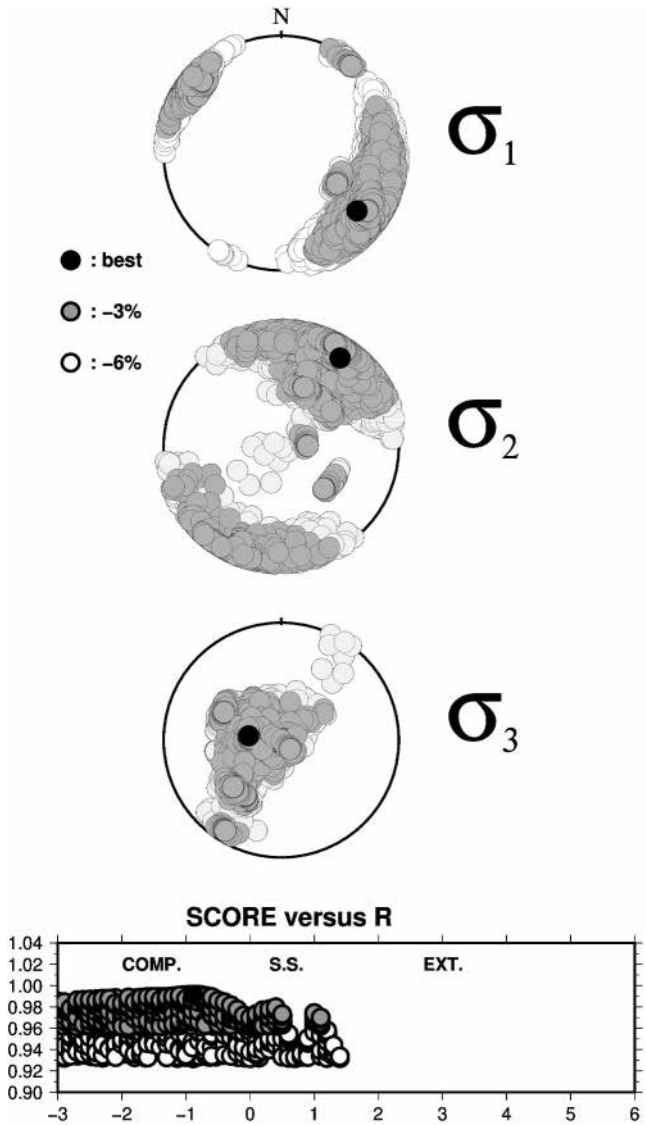

Figure 7. Stress tensor inversion for the 2019 Le Teil sequence (the mainshock and the 19 aftershocks of Figure 6) with exploration of the parameter space. Solutions for σ_1, σ_2, and σ_3 are plotted in three lower hemisphere equal-area projections. The best solution (best score 0.99) is represented by the black dot. The score is the average of the scalar products between observed and computed slip vectors (maximum theoretical best value = 1). Solutions with a score degraded by less than 3% and 6% are represented by gray and open circles, respectively. At the bottom, the same solutions are plotted as a function of their R and score values. We use the same definition for the shape factor R as in Rivera and Cisternas (1990). The domains corresponding to the compressional ($R < 0$), strike-slip ($0 < R < 1$) and extensional ($R > 1$) regimes are labeled COMP., S.S, and EXT., respectively.

5.3. Geology of Epicentral Area

The high level of knowledge of the regional geology has been completed by field works in order to propose a precise framework for the geometry of the active fault plane and the lithology and rheology of the ruptured geological layers. The dip of the La Rouvière active fault, discussed by Ritz et al. (2020) and Marconato et al. (2022), has been precised along strike thanks to field data and with new seismic reflection data along the Escoutay valley, south of the epicentral area (Figure 8a; Thomasset et al., 2024). We conclude that the dip is constant, about 60° toward the SE, from the surface to a depth of at least 2 km. We investigated several other faults located in the epicentral area (Pontet de Couloubre, Mont Faucon, Bayne-Roche Renard, Paurière and Bayne-Saint Alban, Figure 8a) but found no surface evidence of rupture associated with the 11 November 2019 earthquake. On the surface, the trace of the La Rouvière fault is quite simple and continuous: along the zone ruptured in 2019, the fault trace is quite straight for about 5 km, and at both ends of the co-seismic rupture, the trace of the fault bends to the south at the southwestern tip (44.507°N–4.638°E, Figure 6a) and to the north at the northeastern tip (44.533°N–4.675°E).

To identify rock formations where the mainshock and aftershocks nucleated, we must determine the lithology at focal depths. Large regional variations of layer thickness and lithology are indicated by the boreholes of Valvignières and Villeneuve de Berg (e.g., Elmi et al., 1996). Nevertheless, at the scale of the epicentral area from our field investigations the geological layers can be considered to be of relatively constant thickness and homogeneous lithology (Figure 8b). From the surface down to 2 km depth, sedimentary layers of early Cretaceous (Barremian, Hauterivian, Valanginian) and late Jurassic ages dip gently 5–10° to the northwest. Four compartments are bounded by the NE-SW striking major faults (Pontet de Couloubre, La Rouvière, Bayne-Saint Alban) and only the southern compartment displays significant internal deformation with a large synclinal fold (Figure 8b). The in-depth sedimentary sequence of the epicentral area consists of 300 m of massive limestone (Urgonian facies, Barremian age) overlying more than 1200 m of marly limestone (Early Barremian and Hauterivian age), including several compact carbonate beds tens of meters thick. Below this, the 900 m thick Valanginian rocks are made of homogeneous marls with numerous centimeters-thick calcarenitic beds distributed throughout the Valanginian formation. A 50–100 m thick calcarenite layer, the so-called "Laminites de Mirabel" (Elmi et al., 1996), is interbedded in the central part of the Valanginian sequence. These early Cretaceous sedimentary layers are underlain by massive limestone of late Jurassic age (Figure 8b).

In addition, the position of the top of the Valanginian marls layer proposed in our cross-section is consistent with the depth of the sharp Vs inversion in the VM2 velocity model (Figure S3 in Supporting Information S1) attributed by Causse et al. (2021) to a low velocity layer made of less competent material such as claystone.

6. Discussion

6.1. Mainshock: Comparison With Other Slip and Source Models

Several slip models have been published based on the inversion of the InSAR data (Cornou et al., 2021; De Novellis et al., 2020; Marconato et al., 2022; Vallage et al., 2021). All models, and ours, coincide well in rupture length (~4 km), location, shallow depth, and maximum slip value (~30 cm), indicating that these properties are well constrained by the InSAR data. Our result is the first combining InSAR and seismological data. We note the

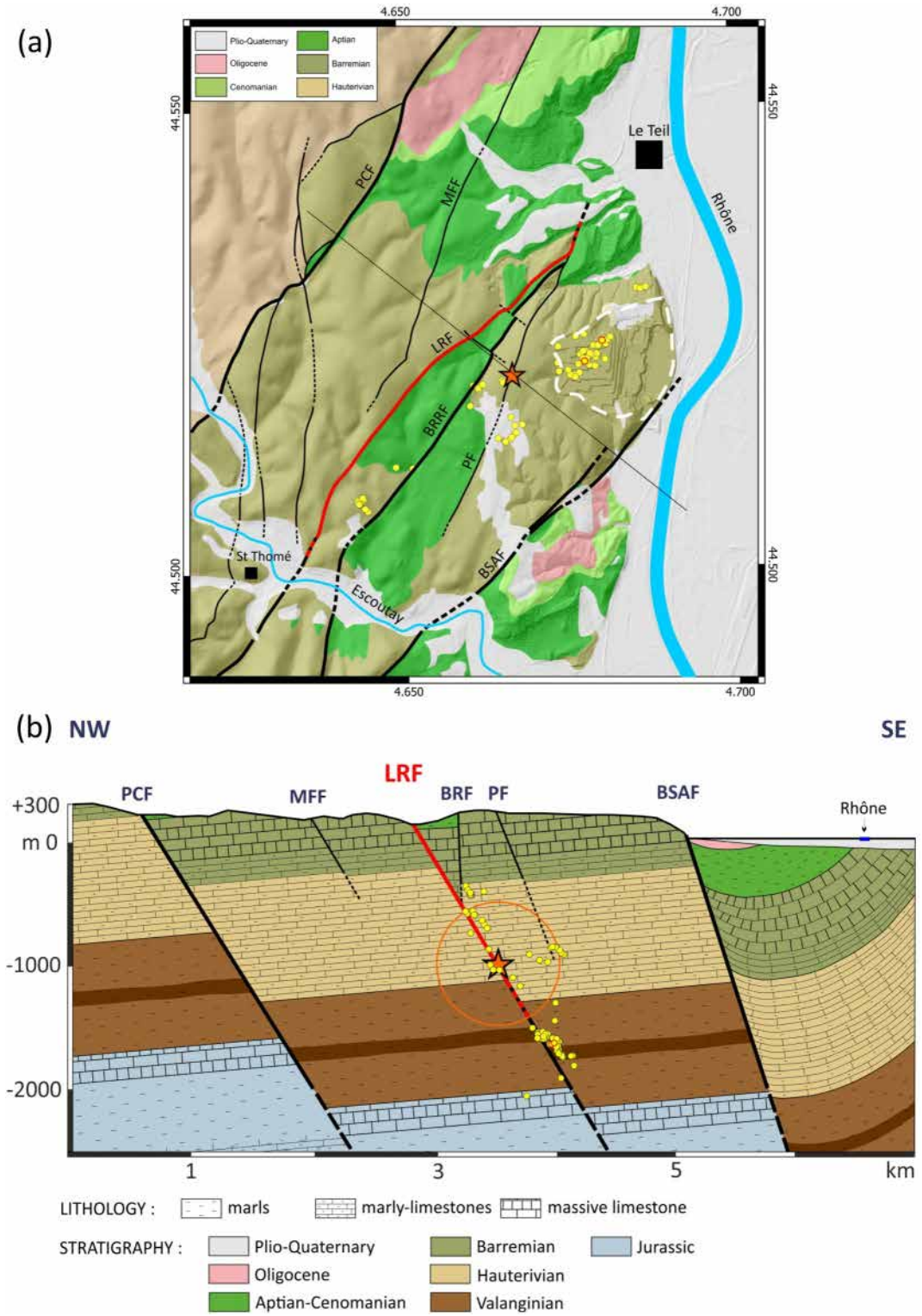

Figure 8. (a) Geological map of the Le Teil area (modified from Elmi et al., 1996). Orange star: mainshock epicenter. Yellow dots: aftershock epicenters; the two main aftershocks (M_L 2.5 and 2.4) are outlined in red. White dashed line: outline of the cement quarry. PCF: Pontet de Couloubre fault, MFF: mont Faucon fault, LRF:La Rouvière fault, BRF: Bayne-Roche Renard fault, PF: Paurière Fault, BSAF: Bayne-Saint Alban fault. Black line: location of the geological cross-section (b). (b) Cross-section striking N135. Orange circle: uncertainty of the focal depth. Red line: activated part of LRF. Yellow dots: projection of the aftershocks on the N135 section. The brown layer within the Valanginian marly sequence corresponds to the presumed location of the so-called "Laminites de Mirabel" made of 50–100 m thick resistant calcarenite.

good compatibility between the two kinds of data and, for the first time, provide a complete picture of the rupture process of the earthquake in space and time. Mordret et al. (2020) estimated some of the kinematic parameters of the earthquake using a new method, seismic stereometry, based on waveform data from two closely spaced stations located about 90 km southeast of the earthquake. Their findings, a dominant lateral propagation to the NE and a rupture velocity of 2.8 km/s disagree with our results based on a much larger and more local seismological data set. Although we do not have all the elements to explain the reasons for such a disagreement, we note that a rupture velocity fixed at 2.8 km/s considerably degrades the waveform fit on the nearby seismological stations (Figure S4 in Supporting Information S1). Furthermore, a dominantly NE propagation of the rupture implies a hypocenter located near the southwestern end of the rupture, a position hardly compatible with the results of the hypocenter relocation (Delouis et al., 2021).

6.2. On the Rate and Decay of Aftershocks

The fit of the Omori-Utsu law to the aftershocks sequence in Section 5.2.1 yielded $K = 22$, $c = 1.25$ day, and $p = 0.95$. The productivity parameter K is related to the number of earthquakes in the sequence and depends exponentially on the mainshock magnitude (Hainzl & Marsan, 2008). However, it also depends on the magnitude of completeness, thus interpretation of the K value is non-trivial. The delay parameter c is generally much less than 1 day, in the order of one to several minutes (Lengliné & Ampuero, 2015); larger values are reported to be related to incomplete detection of aftershocks immediately after the mainshock (Kagan, 2004). A value of 1.25 day (30 hr) may be related to such a missed-detection effect. Indeed, the stations used for template matching started to operate during the day on 12 November and consequently there is a lack of seismicity in the catalog on 11 November. The exponent p falls in the typical range 0.8–1.2 (Utsu et al., 1995), which indicates that Le Teil aftershocks follow the usual decay of aftershock sequences.

We compare the seismicity rate of the aftershock sequence with the Reasenberg-Jones aftershock model (RJ model hereinafter, Reasenberg & Jones, 1994) established for aftershock sequences in California (Figure S16 in Supporting Information S1). For a mainshock of magnitude 4.9 and a magnitude of completeness of −0.5, the RJ model predicts an aftershock rate 100 times higher than that observed for the Le Teil earthquake. This estimation clearly demonstrates that the number of aftershocks following Le Teil earthquake is significantly low. Such observation is also corroborated by the last earthquakes in France with magnitude 5, like Epagny earthquake (1996, M_L 5.3, Thouvenot et al., 1998), Saint Paul de Fenouillet earthquake (1996, $M_L = 5.2$, Rigo et al., 1997) or Rambervillers earthquake (2003, $M_L = 5.4$, Cara et al., 2005) that produced much more aftershocks (several hundred in the months following the mainshock) than the Le Teil earthquake. These observations show that the rate of aftershocks following moderate earthquakes in an equivalent tectonic context can be highly variable, by a factor of 10 for a M5 mainshock.

The b-value of 0.62 computed in Section 5.2.1 is significantly smaller than the usual value of 1. The b-value reflects the relative proportion of the number of large versus small earthquakes. Consequently, the low b-value of Le Teil aftershock sequence could indicate a relative deficit of low magnitude earthquakes. However, this b-value has to be considered with caution. Herrmann and Marzocchi (2020) have shown that b-values computed on high-resolution earthquake catalogs, as those coming from template matching, are usually biased. Moreover, the lack of low magnitude aftershocks could be related to the high noise level in the data (Section 5.2.1) that prevents the detection of small events by template matching.

6.3. Spatial Distribution of Aftershocks and Relation With the Mainshock

Double difference location (Section 5.2.2) reveals that most aftershocks of the Le Teil earthquake are distributed on a SW-NE plane with a 60°SE dip. Such a geometry is corroborated by the fault plane solutions computed in Section 5.2.3. Only few events are off-plane, shifted by 200–500 m to the southeast. Given the small double-difference location uncertainty of 10 m horizontally and vertically, we are quite confident in this distribution of aftershocks.

These results raise the question of whether this plane of aftershocks underlines the fault plane of the mainshock, or whether aftershocks occurred on a subparallel fault plane. Previous studies have determined that the mainshock occurred on a plane striking in the range N45-N50 and dipping toward SE in the range 45°–60° (Cornou et al., 2021; Delouis et al., 2021; Marconato et al., 2022; Ritz et al., 2020; Vallage et al., 2021), compatible with the plane of aftershocks. Considering the location uncertainty of the mainshock (around 500 m horizontally and

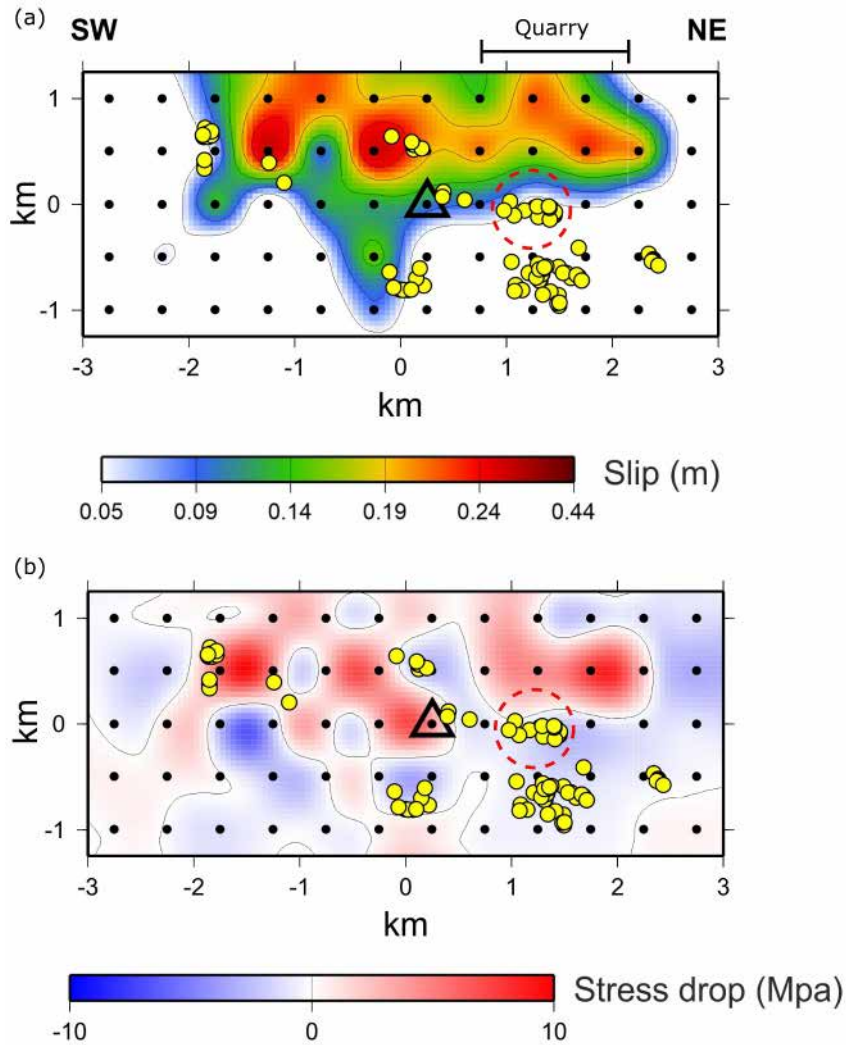

Figure 9. (a) Co-seismic slip distribution of the mainshock (same as in Figure 3e). (b) Along dip shear stress drop distribution. Yellow circles: projection of the aftershocks on the fault plane. Dashed red circle: off-fault aftershocks.

vertically; Delouis et al., 2021) and that of the cloud of aftershocks (around 160 m horizontally and vertically, Section 5.2.2), we cannot formally conclude that mainshock and aftershocks occurred on two different parallel fault planes. We thus adopt the simple assumption of a unique plane.

Such assumption is supported by Figure 9a which displays the superimposition of the aftershocks onto the slip distribution of the mainshock. Most of the aftershocks are located on the borders and outside the mainshock slip area. The same spatial distribution between on-fault aftershocks and mainshock slip has been already observed in numerous cases. In their review of several large earthquakes, Das and Henry (2003) found that large slip areas have generally few and small aftershocks, and that aftershocks tend to cluster at the edges of the ruptured fault and in areas of low slip. The same pattern is also observed for four crustal strike-slip earthquakes in California and Japan (Woessner et al., 2006), for the 2009 L'Aquila Earthquake (Valoroso et al., 2014) and for large earthquakes in subduction zones (Wetzler et al., 2018). Das and Henry (2003) and Rietbrock et al. (2012), also noticed a concentration of aftershocks in regions of rapid transition between high and low slip.

Modeling of the co-seismic shear stress drop (Figure 9b) provides a mechanical explanation for the above observations. Details of the modeling method are described in Text S4 in Supporting Information S1. On the one hand, the shear stress drops are in the order of 5–10 MPa in fault areas experiencing large slip during the mainshock (positive stress drop values in Figure 9b). The resulting low shear stress level is thus no longer

sufficient to enable further rupture during the aftershock sequence. On the other hand, shear stress is transferred toward the edge and outside of the mainshock rupture area, where it increases in the order of 5 MPa (negative stress drop values in Figure 9b). The aftershocks are then promoted in these stressed areas.

We notice that half of the aftershocks are clustered in the northeastern part of the fault plane between 1.5 and 2 km depth, under a large limestone quarry, while in the southwestern part, at the same depth and in an area with similar stress increase, no aftershocks were recorded. This observation raises the question of the possible mechanical role played by the quarry mass withdrawal in enhancing the susceptibility to earthquake triggering during the aftershock sequence. A related question was already addressed for the triggering of the mainshock (De Novellis et al., 2020, 2021; Liang & Ampuero, 2020).

Lastly, we interpret the small cluster of aftershocks separated from the mainshock fault plane in Figure 6b (and red circled in Figure 9), as off-fault seismicity occurring on a secondary fault activated by the mainshock. Das and Henry (2003) noticed the occurrence of such off-fault aftershocks, clearly spatially separated from the on-fault seismicity. They explained that by (a) stress reduction in regions immediately adjacent to the fault and (b) stress increase in remote regions that promotes rupture of preexisting favorably oriented weak planes. Given its location, the off-fault cluster on Figure 6b could therefore be related to stress transfer on the deep part of the Paurière fault. Another possibility would be the off-fault seismicity underlines the branching of the fault structure into a set of conjugate faults at shallow depth, as observed in Valoroso et al. (2014) and Shelly (2020).

6.4. Fault Geometry and Lithology Control on the Mainshock Rupture Nucleation and Propagation

The rupture started near the middle of the straight part of the La Rouvière fault (Figures 3 and 6) and propagated bilaterally (Figure 4) until it reached the SW and NE bends of the fault plane at the surface. It can be assumed that the geometry of the fault plane at the surface is the same at the focal depth (1 km), and it is therefore proposed that the rupture stopped against the two bends of the fault plane.

Taking into account the uncertainty on the focal depth, the field and borehole data show that the 2019 Le Teil earthquake nucleated in the thick marly-limestones series of Hauterivian age and not in the compact high-strength massive limestones of Barremian or late Jurassic age, located in the upper part and in the lower part of the section, respectively (Figure 8b). The location of rupture nucleation and the heterogeneity of the sedimentary series raise two issues:

1. The mechanical behavior of similar rocks (nature and age) in a similar geological context have been studied by Gratier et al. (2013) few tens of km east of Le Teil. Field and laboratory observations show that such clay-rich marly-limestones are prone to continuously relax part of the tectonic stress with time by deformation processes such as pressure-solution. Such a behavior seems likely to prevent accumulation of elastic strain able to produce the 5-km^2 rupture of a M_w 4.9 earthquake (Figure 3). Following Gratier et al. (2013), the exact composition of the marls and limestones (type and clays content), the state of stress and the possible fluid-rock interactions are important to infer the frictional behavior and the seismogenic potential, but such analysis is beyond the scope of this paper. The Le Teil rupture could therefore nucleate in a competent bed of the Hauterivian marly-limestones and then propagate in weaker layers. The same mechanism was proposed for the 2011 Lorca earthquake in Spain (Niemeijer & Vissers, 2014). Rupture would initiate in competent fractured lenses of protolith (in velocity-weakening conditions) and would propagate in the surrounding velocity-strengthening phyllosilicate-rich gouges. Alternatively, it is known that the tectonic displacement along the La Rouvière fault has been estimated to be in the range of 200 m during tectonic episodes lasting from late Cretaceous (~100 Ma) to Oligocene (~30 Ma; Thomasset et al., 2024). This long deformation history in a thick marly-limestone layer and in an extensional context has contributed to the development of localized fluid circulations and large carbonate recrystallization which are observed in the fault core from samples collected during a drill through the fault (Gébelin et al., 2024). Such carbonate recrystallization can locally increase the rock strength and its capacity for elastic strain accumulation, thereby favoring potential rupture nucleation in this weak sedimentary formation (e.g., Marchesini et al., 2022; Tesei et al., 2014).
2. The finite source inversion shows that most of the rupture propagated upward from the hypocenter (Figure 3). The maximum slip occurred between 500-m-depth and the surface, that is, through the Barremian high-strength massive limestones (Figure 8b). In a simple way, one can consider that the 2-km shallower sedimentary cover has an almost homogeneous NW-SE horizontal compressive state of stress (Heidbach et al., 2018) but the lithological contrast could induce a heterogeneous partitioning of the elastic strain

accumulated in the different layers. On the one hand, the marls/marly-limestones, capable of aseismic creep, progressively relax the stress with time. On the other hand, the massive limestones can accumulate a large amount of elastic strain. Therefore, during the Le Teil earthquake the rupture did not spread very far downwards through the marls layer of Valanginian age (Figure 8b) but propagated upwards. Once the rupture front reached the massive limestones, these could act as a stress reservoir and amplify the rupture propagation, as attested by the largest slip in the ∼500-m shallowest part of the activated fault plane (Figure 3). This observation could explain the apparent paradox of the rupture propagation over a large surface although the earthquake nucleated in a low-strength lithology that accumulates little elastic strain.

6.5. Lithological Control of the Aftershocks Occurrence

We hypothesize that the observed low rate of aftershocks in the Le Teil sequence (Section 6.2) might be directly controlled by lithological properties. Indeed, while the previous magnitude 5 earthquakes in France took place in high-strength rock contexts [massive limestones for Epagny earthquake (1996-07-15, M_L 5.3), granitic and metamorphic rocks for Saint Paul de Fenouillet (1996-02-18, M_L 5.2) and Rambervillers (2003-02-22, M_L 5.4) earthquakes], the Le Teil earthquake sequence mainly took place in soft rocks (Sections 5.3 and 6.3). As shown on Figure 8b, the aftershocks are essentially located in marly-limestones (early Barremian and Hauterivian ages) and marls (Valanginian age). Hence, most of the postseismic strain in marls and marly limestones shall be accommodated by aseismic creep since, as discussed in Section 6.4, this is the dominant deformation mechanism in such lithologies (e.g., Gratier et al., 2013). Only a small fraction of the deformation would then be seismically accommodated by ruptures of limestone layers, such as the "laminites de Mirabel" and other thinner calcarenitic beds, intercalated in marls. We test this hypothesis by estimating the magnitude range that could be produced by ruptures in such limestone layers and comparing them with the magnitude of the aftershocks. For this purpose, we consider a simple circular crack model (Eshelby, 1957), for which the seismic moment M_0 for given rupture radius r and stress drop $\Delta\sigma$ is

$$M_0 = \frac{16}{7}\Delta\sigma r^3 \tag{4}$$

Our field observations show that the thickness of limestones and calcarenite layers varies between 0.1 and 100 m. Considering that ruptures are confined within these layers, along planes dipping around 60° (based on mainshock plane dip and focal mechanisms of aftershocks), we infer rupture diameters ranging between 0.12 and 115 m. Applying Equation 4, assuming a stress drop varying in the range 0.1–10 MPa (e.g., Abercrombie, 1995) and considering the moment magnitude scale of Hanks and Kanamori (1979), we find equivalent magnitudes ranging between −4.9 and 1.1 for the thinnest layers and −3.6 and 2.4 for the thickest layers. These values agree with the magnitude of the recorded aftershocks. Thus, these results validate the hypothesis that the aftershocks could be produced by fractures of the limestone layers embedded in marls.

More specifically, the two main aftershocks of magnitude 2.5 and 2.4 would require ruptures in limestones layers over 100 m thick. With a stress drop larger than 10 MPa, the required layer thickness might be somewhat smaller. In the Valanginian marls sequence, only the layer of calcarenite which is 50–100 m thick ("Laminites de Mirabel") seems able to nucleate these two aftershocks. For instance, it has been suggested that rheological heterogeneities associated with lithological variations at the base of the seismogenic zone control the location of clusters of deep aftershocks following the 2016–2017 seismic sequence in central Italy (Volpe et al., 2023). Another possibility is that the two largest aftershocks broke a limestone layer much thinner than 100 m and then propagated horizontally, developing into a non-circular, elongated rupture. Alternatively, multiple thin layers of limestone could break jointly despite the intervening marl. Hence a rupture cascade starting in a limestone layer, could dynamically trigger the next limestone layer, and so on, so that the cumulative rupture reaches an effective length greater than 100 m. Such rupture cascades have been recently observed by DAS along a borehole fiber optic cable, in a different context of englacial quakes on a fast-flowing glacier in Greenland (Fichtner et al., 2025).

6.6. Relation Between Faults and Seismicity

As discussed in Section 6.3, the mainshock and most of the aftershocks likely occurred on a unique plane striking SW-NE and dipping 60°SE. Considering (a) the uncertainty on the location of the mainshock and of the cloud of aftershocks (a few hundred meters in horizontal and vertical, Section 6.3) and (b) the surface trace (∼50N,

Figure 8a) and dip (~60–70°) of the main fault in the epicentral area (Marconato et al., 2022; Ritz et al., 2020; Thomasset et al., 2024), we conclude that most of the seismicity (mainshock and aftershocks) occurred on the La Rouvière Fault (Figure 6b). This corroborates conclusions of the previous studies stating that the Le Teil earthquake resulted from the reactivation of the La Rouvière fault (Marconato et al., 2022; Ritz et al., 2020; Vallage et al., 2021).

In addition, shallow seismicity (above 1 km depth) may also have occurred at the junction between the La Rouvière and Bayne-Roche Renard faults (BRF, Figures 6b and 8b). Finally, the few off-fault aftershocks shown in Section 6.3 could be related to the Paurière fault (PF, Figures 6b and 8b).

6.7. Inversion of the La Rouvière Fault

Morphotectonic data shows that the long-term kinematics of the La Rouvière fault and other regional faults that bound the western edge of the South-East basin of France is mainly normal since the Oligocene (Figure 1; Roure et al., 1992; Bonijoly et al., 1996; Ritz et al., 2020; Marconato et al., 2022; Thomasset et al., 2024). The present-day tectonic inversion of the La Rouvière fault from normal to reverse is clearly attested by the pure reverse faulting focal mechanism of the 2019 earthquake (Delouis et al., 2021; this paper) and the consistent kinematics observed at the surface (Ritz et al., 2020).

Inversion of normal faults is observed in former extensional basins that later contracted during compressional phases (e.g., Cooper & Warren, 2020; Turner & Williams, 2004). Reactivation of normal faults under compression requires specific geometrical and mechanical conditions (e.g., Collettini et al., 2019; Copley, 2018; Sibson & Xie, 1998). The inversion during the Le Teil earthquake is therefore emblematic because the high-angle 60°-dip rupture plane is theoretically severely misoriented for typical values of fault friction coefficient >0.6 (Sibson, 1994). However, the reactivation angle between the rupture plane and σ_1 is actually around 40° due to the 20°SE plunge of σ_1 (Section 5.2.3 and Figure 7). Thus, such a value tends toward the theoretical angle of 30° between thrust-fault and σ_1. Furthermore, weakening of fault zones crossing through marly-limestone rich-lithologies is facilitated by the concentration and the reorganization of phyllosilicates minerals along shear surfaces which helps to reduce the friction coefficient on the fault to values in the range 0.2–0.3 (e.g., Lacroix et al., 2015; Rutter et al., 2001). In a borehole drilled across the La Rouvière fault, intersecting the fault plane at a depth of 25 m, we found a ~1 cm-thick gouge. It is reasonable to suggest that such a gouge lies over a large part of the fault surface.

Therefore, despite an apparent severe misorientation, conditions are met for the La Rouvière normal fault to be inverted by the present-day compressional stress regime. At this stage, there is no clear explanation for the current state of stress, in particular the southeastward tilt of σ_1.

7. Conclusions

The joint seismological and geological analysis presented here, clearly demonstrates the close link between the lithological features, rheology and seismicity during the 2019 M_w 4.9 Le Teil earthquake sequence. (a) The determination of the co-seismic slip kinematic model for the mainshock by joint inversion of InSAR and seismological data, (b) the detailed analysis of the aftershocks (template matching detection, high precision location, determination of focal mechanisms) and (c) the precise repositioning of seismicity in the local geological context, provide several main insights depicted in Figure 10 and summarized below:

- The co-seismic slip of the mainshock is confined above 1.5 km depth, with a maximum above 0.6 km depth. Rupture propagated up-dip and bilaterally horizontally. The rupture nucleation and propagation seem to be controlled by the lithology. The rupture nucleated around 1 km depth in a thick marly-limestone layer and propagated up-dip through a surficial massive limestone layer. The amount of co-seismic slip could be related to the contrasted rheology of these two layers with a maximum above 0.5 km depth related to the better ability of the massive limestones to store elastic strain.
- 115 aftershocks are identified between 12 November and 13 January, which is low for an earthquake of such magnitude. Such low aftershock productivity may be related to the weak layers of marls and marly-limestones at focal depths. The few aftershocks might actually occur in competent beds of limestones of varying thickness, intercalated in marls.

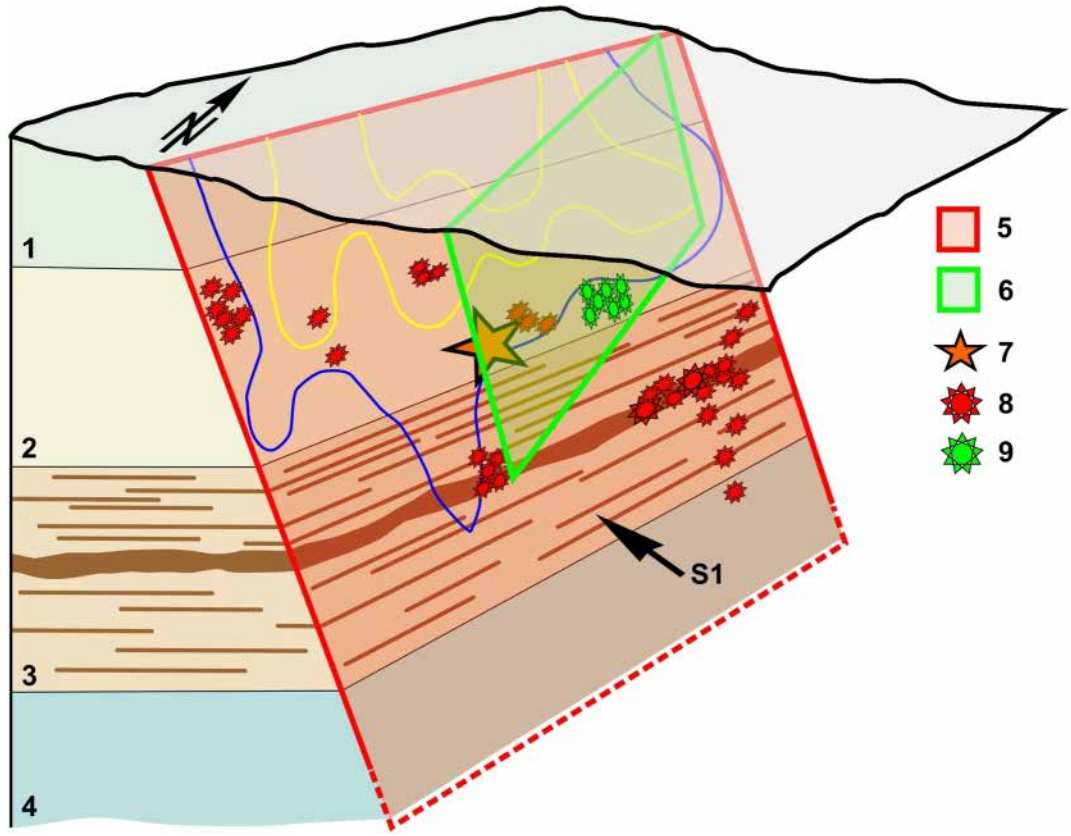

Figure 10. Conceptual sketch (not at scale) designed to highlight the relationships between (i) the lithology (1: massive limestone, 2: marly-limestone, 3: marls and calcarenite beds, 4: massive limestone), (ii) the faults (5: La Rouvière fault, 6: the Paurière fault) and the foci (7: mainshock, 8: aftershocks on the La Rouvière fault and 9: aftershocks on the Paurière fault). The yellow and blue curves are the 12 and 20 cm approximative slip contours, respectively (from Figure 3e). For simplicity, the Baynes-Roche Renard fault is not represented.

- The aftershocks clearly delineate a 4 km-long NE-SW plane with a 60° dip toward the SE, consistent with the extent and the geometry of the La Rouvière fault activated during the mainshock. The focal mechanisms show a remarkable homogeneity: they all correspond to reverse faulting with NE-SW strike and a nodal plane dipping around 60° toward SE, compatible with the alignment of the seismicity. Furthermore, their focal mechanisms are similar to that of the mainshock.
- Despite an a priori misorientation, the inversion of the high-angle (60°SE dip) La Rouvière normal fault during the mainshock and aftershocks is facilitated by (a) the plunge of the compressional axis σ_1 by 20°SE, which reduces the angle between the fault plane and σ_1 to 40°, and (b) the presence of a clay gouge on the fault plane found by drilling at 25 m depth and probably extending over a large part of the fault plane.

To fully understand this emblematic earthquake, many questions remain about the mechanical parameters of the rocks at focal depth. Drilling through active faults is essential to correlate the structure, mineralogy and fluids of the fault zone with its slip behavior. The extremely shallow nature of the Le Teil earthquake offers an exceptional opportunity to drill across the fault at the hypocentral depth of a significant recent earthquake. The next objective is to drill to a depth of 1.5 km to measure the physical properties of the rock environment and to collect samples in the nucleation zone for laboratory analysis.

Data Availability Statement

The seismological data used in this study are available on Epos-France data portal (https://seismology.resif.fr) under the network code FR (Epos-France, 1995), RA (RESIF, 1995) and 3C (Bertrand et al., 2019). The code used

to compute stress drop (Arzu, 2025) in Section 6.3 is available in a public repository (https://zenodo.org/records/15172382). It includes instructions to easily reproduce the stress drop figure (Figure 9b) shown in the paper.

Acknowledgments
This work was carried out in the context of the CNRS-INSU Fremteil project. We are grateful to Epos-France for making seismological records available and the people that installed and maintained the post-seismic temporary networks. We are also grateful to the EDF (Electricité de France) and SNCF company (Société Nationale des Chemins de fer Français) for providing access to seismological records in the vicinity of the Le Teil earthquake. SNCF data were made available to us with the help of the IRSN (Institut de Radioprotection et de Sûreté Nucléaire). We are grateful to the Lafarge-Holcim cement company who gave us access to the records of the geophone sensor placed in the private house of the Clauzel familly, and to the Clauzel themselves who received the seismologists at home with great kindness. A great thanks to Raphaël Grandin, Olivier Cavalié and Romain Jolivet who gave us access to the processed InSAR data. We would like to thank S. Pouliquen of EDF for sharing the results of the recent seismic survey along the Escoutay valley. Finally, we thank the Editor Alexandre Schubnel, the anonymous Associate Editor and the two reviewer Patricia Martínez-Garzón Cristiano Collettini for their constructive comments. We also thank C. Collettini for suggesting several targets for future research.

References

Abercrombie, R. E. (1995). Earthquake source scaling relationships from 1 to 5 M_L using seismograms recorded at 2.5-km depth. *Journal of Geophysical Research*, *100*(B12), 24015–24036. https://doi.org/10.1029/95JB02397

Aki, K. (1965). Maximum likelihood estimate of b in the formula log n = a-bm and its confidence limits. *Bull. Earthquake Res. Inst., Tokyo Univ.*, *43*, 237–239.

AlpArray Seismic Network. (2015). *AlpArray Seismic Network (AASN) temporary component*. AlpArray Working Group. https://doi.org/10.12686/alparray/z3_2015

Ampuero, J. P., Billant, J., Brenguier, F., Cavalié, O., Courboulex, F., Deschamps, A., et al. (2020). The November 11 2019 Le Teil, France M5 earthquake: A triggered event in nuclear country. In *EGU general assembly 2020*. https://doi.org/10.5194/egusphere-egu2020-18295

Arzu, F. (2025). Compute Stress Drop for a given Slip Distribution for the Le Teil Earthquake (Mw4.9, 2019/11/11, France) [Software]. *Journal of Geophysical Research - Solid Earth. Zenodo*. https://doi.org/10.5281/zenodo.15172382

Baize, S., & Ritz, J. F. (2022). Post-publication careers: Ground ruptured, community united. *Communications Earth & Environment*, *3*(1), 61. https://doi.org/10.1038/s43247-022-00392-y

Baques, M., DeBarros, L., Godano, M., Duverger, C., & Jomard, H. (2023). Swarms and mainshock aftershocks sequences are both triggered by fluids in the Ubaye Region (Western Alps). *Geophysical Journal International*, *235*(1), 920–941. https://doi.org/10.1093/gji/ggad280

Barchi, M., Carboni, F., Michele, M., Ercoli, M., Giorgetti, C., Porreca, M., et al. (2021). The influence of subsurface geology on the distribution of earthquakes during the 2016-2017 central Italy seismic sequence. *Tectonophysics*, *807*, 228797. https://doi.org/10.1016/j.tecto.2021.228797

BCSF-Rénass. (2022). *Instrumental seismicity in mainland France (1962-2021)*. EOST UAR830, Université de Strasbourg, CNRS. (Collection). https://doi.org/10.25577/fv3f-sq09

Bertrand, E., Cornou, C., Gélis, C., & Rivet, D., & SISMOB-RESIF. (2019). Le Teil P5 post seismic experiment [Dataset]. *RESIF - Réseau Sismologique et géodésique Français*. https://doi.org/10.15778/resif.3c2019

Blès, J., & Gros, Y. (1991). Stress field changes in the Rhone valley from the Miocene to the present. *Tectonophysics*, *194*(3), 265–277. https://doi.org/10.1016/0040-1951(91)90264-S

Bocchini, G. M., Martínez-Garzón, P., Verdecchia, A., Harrington, R. M., Bohnhoff, M., Turkmen, T., & Nurlu, M. (2022). Direct evidence of a slow-slip transient modulating the spatiotemporal and frequency-magnitude earthquake distribution: Insights from the Armutlu Peninsula, northwestern Turkey. *Geophysical Research Letters*, *49*(18), e2022GL099077. https://doi.org/10.1029/2022GL099077

Bollinger, L., Dortz, K. L., Duverger, C., Vallage, A., Marin, S., & Leroy, Y. M. (2021). Seismic swarms in Tricastin, lower Rhône Valley (France): Review of historical and instrumental seismicity and models. *Comptes Rendus Geoscience*, *353*(S1), 585–606. https://doi.org/10.5802/crgeos.93

Bonijoly, D., Perrin, J., Roure, F., Bergerat, F., Courel, L., Elmi, S., & Mignot, A. (1996). The Ardèche palaeomargin of the South-East basin of France: Mesozoic evolution of a part of the Tethyan continental margin (Géologie profonde de la France programme). *Marine and Petroleum Geology*, *13*(6), 607–623. https://doi.org/10.1016/0264-8172(95)00075-5

Bouchon. (1981). A simple method to calculate Green's functions for elastic layered media. *Bulletin of the Seismological Society of America*, *71*(4), 959–971. https://doi.org/10.1785/BSSA0710040959

Burnol, A., Armandine Les Landes, A., Raucoules, D., Foumelis, M., Allanic, C., Paquet, F., et al. (2023). Impacts of water and stress transfers from ground surface on the shallow earthquake of 11 November 2019 at Le Teil (France). *Remote Sensing*, *15*(9), 2270. https://doi.org/10.3390/rs15092270

Calais, E., Camelbeeck, T., Stein, S., Liu, M., & Craig, T. (2016). A new paradigm for large earthquakes in stable continental plate interiors. *Geophysical Research Letters*, *43*(20), 10–621. https://doi.org/10.1002/2016GL070815

Canitano, A., Godano, M., & Thomas, M. Y. (2021). Inherited state of stress as a key factor controlling slip and slip mode: Inference from the study of a slow slip event in the longitudinal valley, Taiwan. *Geophysical Research Letters*, *48*(3), e2020GL090278. https://doi.org/10.1029/2020GL090278

Cara, M., Brüstle, W., Gisler, M., Kästli, P., Sira, C., Weihermüller, C., & Lambert, J. (2005). Transfrontier macroseismic observations of the M_L = 5.4 earthquake of February 22, 2003 at Rambervillers, France. *Journal of Seismology*, *9*(3), 317–328. https://doi.org/10.1007/s10950-005-6853-1

Carminati, E., Bignami, C., Doglioni, C., & Smeraglia, L. (2020). Lithological control on multiple surface ruptures during the 2016-2017 Amatrice-Norcia seismic sequence. *Journal of Geodynamics*, *134*, 101676. https://doi.org/10.1016/j.jog.2019.101676

Causse, M., Cornou, C., Maufroy, E., Grasso, J.-R., Baillet, L., & El Haber, E. (2021). Exceptional ground motion during the shallow Mw 4.9 2019 Le Teil earthquake, France. *Communications Earth & Environment*, *2*(1), 14. https://doi.org/10.1038/s43247-020-00089-0

Chantraine, J., Autran, A., & Cavelier, C. (2003). Carte géologique de la France (version numérique) à l'échelle du millionième. BRGM, Orléans, 6ème edition.

Collettini, C., Barchi, M. R., De Paola, N., Trippetta, F., & Tinti, E. (2022). Rock and fault rheology explain differences between on fault and distributed seismicity. *Nature Communications*, *13*(1), 5627. https://doi.org/10.1038/s41467-022-33373-y

Collettini, C., Tesei, T., Scuderi, M., Carpenter, B., & Viti, C. (2019). Beyond Byerlee friction, weak faults and implications for slip behavior. *Earth and Planetary Science Letters*, *519*, 245–263. https://doi.org/10.1016/j.epsl.2019.05.011

Cooper, M., & Warren, M. J. (2020). Chapter 10 - Inverted fault systems and inversion tectonic settings. In N. Scarselli, J. Adam, D. Chiarella, D. G. Roberts, & A. W. Bally (Eds.), *Regional geology and tectonics* (2nd ed., pp. 169–204). Elsevier. https://doi.org/10.1016/B978-0-444-64134-2.00009-2

Copley, A. (2018). The strength of earthquake-generating faults. *Journal of the Geological Society*, *175*(1), 1–12. https://doi.org/10.1144/jgs2017-037

Cornou, C., Ampuero, J.-P., Aubert, C., Audin, L., Baize, S., Billant, J., et al. (2021). Rapid response to the Mw 4.9 earthquake of November 11, 2019 in Le Teil, Lower Rhône Valley, France. Comptes Rendus. *Geoscience*, *353*(S1), 441–463. https://doi.org/10.5802/crgeos.30

Das, S., & Henry, C. (2003). Spatial relation between main earthquake slip and its aftershock distribution. *Reviews of Geophysics*, *41*(3). https://doi.org/10.1029/2002RG000119

De Barros, L., Baques, M., Godano, M., Helmstetter, A., Deschamps, A., Larroque, C., & Courboulex, F. (2019). Fluid-induced swarms and coseismic stress transfer: A dual process highlighted in the aftershock sequence of the 7 April 2014 earthquake (M_L 4.8, Ubaye, France). *Journal of Geophysical Research: Solid Earth*, *124*(4), 3918–3932. https://doi.org/10.1029/2018JB017226

De Barros, L., Cappa, F., Deschamps, A., & Dublanchet, P. (2020). Imbricated aseismic slip and fluid diffusion drive a seismic swarm in the Corinth Gulf, Greece. *Geophysical Research Letters*, *47*(9), e2020GL087142. https://doi.org/10.1029/2020GL087142

Delouis, B., Déverchère, J., Melnikova, V., Radziminovitch, N., Loncke, L., Larroque, C., et al. (2002b). A reappraisal of the 1950 (Mw 6.9) Mondy earthquake, Siberia, and its relationship to the strain pattern at the southwestern end of the Baikal rift zone. *Terra Nova*, *14*(6), 491–500. https://doi.org/10.1046/j.1365-3121.2002.00445.x

Delouis, B., Giardini, D., Lundgren, P., & Salichon, J. (2002a). Joint inversion of InSAR, GPS, teleseismic and strong motion data for the spatial and temporal distribution of earthquake slip: Application to the 1999 Izmit mainshock. *Bulletin of the Seismological Society of America*, *92*(1), 278–299. https://doi.org/10.1785/0120000806

Delouis, B., Oral, E., Menager, M., Ampuero, J.-P., Trilla, A. G., Régnier, M., & Deschamps, A. (2021). Constraining the point source parameters of the 11 November 2019 Mw 4.9 Le Teil earthquake using multiple relocation approaches, first motion and full waveform inversions. *Comptes Rendus Geoscience*, *353*(S1), 493–516. https://doi.org/10.5802/crgeos.78

De Novellis, V., Convertito, V., Valkaniotis, S., Casu, F., Lanari, R., Monterroso Tobar, M. F., & Pino, N. A. (2020). Coincident locations of rupture nucleation during the 2019 Le Teil earthquake, France and maximum stress change from local cement quarrying. *Communications Earth & Environment*, *1*(1), 20. https://doi.org/10.1038/s43247-020-00021-6

De Novellis, V., Convertito, V., Valkaniotis, S., Casu, F., Lanari, R., Monterroso Tobar, M. F., & Pino, N. A. (2021). Author correction: Coincident locations of rupture nucleation during the 2019 Le Teil earthquake, France and maximum stress change from local cement quarrying. *Communications Earth & Environment*, *2*(1), 47. https://doi.org/10.1038/s43247-020-00021-6

Elmi, S., Busnardo, R., Clavel, B., Camus, G., Kieffer, G., Bérard, P., & Michaëly, B. (1996). Notice explicative, carte géologique France 1/50000, feuille Aubenas (865). *Orléans: BRGM, 170p. Carte géologique par Y. Kerrien (coord.), S. Elmi, R. Busnardo, G. Camus, G. Kieffer, J. Moinereau, A. Weisbrod (1989)*. http://infoterre.brgm.fr/

Epos-France. (1995). Epos-France Broad-band network (RLBP) [Dataset]. *Epos-France Seismological Data Centre*. https://doi.org/10.15778/resif.fr

Eshelby, J. D. (1957). The determination of the elastic field of an ellipsoidal inclusion, and related problems. *Proceedings of the Royal Society of London. Series A. Mathematical and Physical Sciences*, *241*(1226), 376–396. https://doi.org/10.1098/rspa.1957.0133

Fichtner, A., Hofstede, C., Kennett, B. L. N., Svensson, A., Westhoff, J., Walter, F., et al. (2025). Hidden cascades of seismic ice stream deformation. *Science*, *387*(6736), 858–864. https://doi.org/10.1126/science.adp8094

Ford, M., & Lickorish, W. H. (2004). Foreland basin evolution around the Western Alpine arc. *Geological Society, London, Special Publications*, *221*(1), 39–63. https://doi.org/10.1144/GSL.SP.2004.221.01.04

Gébelin, A., Matonti, C., Larroque, C., Carr, P., & Ampuero, J. P. (2024). First in situ calcite U–Pb dating revealing the past episodes of the 2019 Le Teil Earthquake (France). *Comptes Rendus Geoscience*, *356*(G1), 195–209. https://doi.org/10.5802/crgeos.280

Gibbons, S. J., & Ringdal, F. (2006). The detection of low magnitude seismic events using array-based wave-form correlation. *Geophysical Journal International*, *165*(1), 149–166. https://doi.org/10.1111/j.1365-246X.2006.02865.x

Godano, M., Deschamps, A., Lambotte, S., Lyon-Caen, H., Bernard, P., & Pacchiani, F. (2014). Focal mechanisms of earthquake multiplets in the western part of the Corinth Rift (Greece): Influence of the velocity model and constraints on the geometry of the active faults. *Geophysical Journal International*, *197*(3), 1660–1680. https://doi.org/10.1093/gji/ggu059

Godano, M., Regnier, M., Deschamps, A., Bardainne, T., & Gaucher, E. (2009). Focal mechanisms from sparse observations by nonlinear inversion of amplitudes: Method and tests on synthetic and real data. *Bulletin of the Seismological Society of America*, *99*(4), 2243–2264. https://doi.org/10.1785/0120080210

Grandin, R., Vallée, M., & Lacassin, R. (2017). Rupture process of the Mw 5.8 Pawnee, Oklahoma, earthquake from Sentinel-1 InSAR and seismological data. *Seismological Research Letters*, *88*(4), 994–1004. https://doi.org/10.1785/0220160226

Gratier, J.-P., Thouvenot, F., Jenatton, L., Tourette, A., Doan, M.-L., & Renard, F. (2013). Geological control of the partitioning between seismic and aseismic sliding behaviours in active faults: Evidence from the Western Alps, France. *Tectonophysics*, *600*, 226–242. https://doi.org/10.1016/j.tecto.2013.02.013

Hainzl, S., & Marsan, D. (2008). Dependence of the Omori-Utsu law parameters on main shock magnitude: Observations and modeling. *Journal of Geophysical Research*, *113*(B10). https://doi.org/10.1029/2007JB005492

Hanks, T. C., & Kanamori, H. (1979). A moment magnitude scale. *Journal of Geophysical Research*, *84*(B5), 2348–2350. https://doi.org/10.1029/JB084iB05p02348

Heidbach, O., Rajabi, M., Cui, X., Fuchs, K., Mller, B., Reinecker, J., et al. (2018). The world stress map database release 2016: Crustal stress pattern across scales. *Tectonophysics*, *744*, 484–498. https://doi.org/10.1016/j.tecto.2018.07.007

Herrmann, M., & Marzocchi, W. (2020). Inconsistencies and lurking pitfalls in the magnitude–frequency distribution of high-resolution earthquake catalogs. *Seismological Research Letters*, *92*(2A), 909–922. https://doi.org/10.1785/0220200337

Hetényi, G., Molinari, I., Clinton, J., Bokelmann, G., Bondár, I., Crawford, W. C., et al. (2018). The alparray seismic network: A large-scale European experiment to image the Alpine orogen. *Surveys in Geophysics*, *39*(5), 1009–1033. https://doi.org/10.1007/s10712-018-9472-4

Jacquemond, L., Godano, M., Cappa, F., & Larroque, C. (2024). Interplay between fluid intrusion and aseismic stress perturbations in the onset of earthquake swarms following the 2020 Alex extreme rainstorm. *Earth and Space Science*, *11*(6), e2024EA003528. https://doi.org/10.1029/2024EA003528

Jomard, H., Scotti, O., Auclair, S., Dominique, P., Manchuel, K., & Sicilia, D. (2021). The SISFRANCE database of historical seismicity. State of the art and perspectives. *Comptes Rendus Geoscience*, *353*(S1), 257–280. https://doi.org/10.5802/crgeos.91

Kagan, Y. Y. (2004). Short-term properties of earthquake catalogs and models of earthquake source. *Bulletin of the Seismological Society of America*, *94*(4), 1207–1228. https://doi.org/10.1785/012003098

Lacroix, B., Tesei, T., Oliot, E., Lahfid, A., & Collettini, C. (2015). Early weakening processes inside thrust fault. *Tectonics*, *34*(7), 1396–1411. https://doi.org/10.1002/2014TC003716

Larroque, C., Baize, S., Albaric, J., Jomard, H., Trévisan, J., Godano, M., et al. (2021). Seismotectonics of Southeast France: From the Jura Mountains to Corsica. *Comptes Rendus Geoscience*, *353*(S1), 105–151. https://doi.org/10.5802/crgeos.69

Lengliné, O., & Ampuero, J.-P. (2015). Insights on earthquake triggering processes from early aftershocks of repeating microearthquakes. *Journal of Geophysical Research: Solid Earth*, *120*(10), 6977–6992. https://doi.org/10.1002/2015JB012287

Liang, C., & Ampuero, J.-P. (2020). Comment on coincident locations of rupture nucleation during the 2019 Le Teil earthquake, France and maximum stress change from local cement quarrying by de Novellis et al. ESS Open Archive. https://doi.org/10.1002/essoar.10504400.2

Lomax, A., Virieux, J., Volant, P., & Berge-Thierry, C. (2000). Probabilistic earthquake location in 3d and layered models. In C. H. Thurber & N. Rabinowitz (Eds.), *Advances in seismic event location* (pp. 101–134). Springer Netherlands. https://doi.org/10.1007/978-94-015-9536-0

Manchuel, K., Traversa, P., Baumont, D., Cara, M., Nayman, E., & Durouchoux, C. (2018). The French seismic catalogue (fcat-17). *Bulletin of Earthquake Engineering*, *16*(6), 2227–2251. https://doi.org/10.1007/s10518-017-0236-1

Marchesini, B., Carminati, E., Aldega, L., Mirabella, F., Petrelli, M., Caracausi, A., & Barchi, M. R. (2022). Chemical interaction driven by deep fluids in the damage zone of a seismogenic carbonate fault. *Journal of Structural Geology*, *161*, 104668. https://doi.org/10.1016/j.jsg.2022.104668

Marconato, L., Leloup, P. H., Lasserre, C., Jolivet, R., Caritg, S., Grandin, R., et al. (2022). Insights on fault reactivation during the 2019 November 11, Mw 4.9 Le Teil earthquake in southeastern France, from a joint 3-D geological model and InSAR time-series analysis. *Geophysical Journal International*, *229*(2), 758–775. https://doi.org/10.1093/gji/ggab498

Martínez-Garzón, P., Durand, V., Bentz, S., Kwiatek, G., Dresen, G., Turkmen, T., et al. (2021). Near-fault monitoring reveals combined seismic and slow activation of a fault branch within the Istanbul–Marmara Seismic gAp in Northwest Turkey. *Seismological Research Letters*, *92*(6), 3743–3756. https://doi.org/10.1785/0220210047

Masson, C., Mazzotti, S., & Vernant, P. (2019). Precision of continuous GPS velocities from statistical analysis of synthetic time series. *Solid Earth*, *10*(1), 329–342. https://doi.org/10.5194/se-10-329-2019

Mordret, A., Brenguier, F., Causse, M., Boué, P., Voisin, C., Dumont, I., et al. (2020). Seismic stereometry reveals preparatory behavior and source kinematics of intermediate-size earthquakes. *Geophysical Research Letters*, *47*(17), e2020GL088563. https://doi.org/10.1029/2020GL088563

Neo, J. C., Huang, Y., Yao, D., & Wei, S. (2020). Is the aftershock zone area a good proxy for the mainshock rupture area? *Bulletin of the Seismological Society of America*, *111*(1), 424–438. https://doi.org/10.1785/0120190200

Niemeijer, A. R., & Vissers, R. L. M. (2014). Earthquake rupture propagation inferred from the spatial distribution of fault rock frictional properties. *Earth and Planetary Science Letters*, *396*, 154–164. https://doi.org/10.1016/j.epsl.2014.04.010

Reasenberg, P. A., & Jones, L. M. (1994). Earthquake aftershocks: Update. *Science*, *265*(5176), 1251–1252. https://doi.org/10.1126/science.265.5176.1251

RESIF. (1995). RESIF-RAP French accelerometric network [Dataset]. *RESIF - Réseau Sismologique et géodésique Français*. https://doi.org/10.15778/RESIF.RA

Rietbrock, A., Ryder, I., Hayes, G., Haberland, C., Comte, D., Roecker, S., & Lyon-Caen, H. (2012). Aftershock seismicity of the 2010 Maule Mw=8.8, Chile, earthquake: Correlation between co-seismic slip models and aftershock distribution? *Geophysical Research Letters*, *39*(8). https://doi.org/10.1029/2012GL051308

Rigo, A., Souriau, A., Pauchet, H., Grésillaud, A., Nicolas, M., Olivera, C., & Figueras, S. (1997). The February 1996 earthquake sequence in the Eastern Pyrenees: First results. *Journal of Seismology*, *1*, 3–14. https://doi.org/10.1023/A:1009711512921

Ritz, J.-F., Baize, S., Ferry, M., Larroque, C., Audin, L., Delouis, B., & Mathot, E. (2020). Surface rupture and shallow fault reactivation during the 2019 Mw 4.9 Le Teil earthquake, France. *Communications Earth & Environment*, *1*(1), 10. https://doi.org/10.1038/s43247-020-0012-z

Rivera, L., & Cisternas, A. (1990). Stress tensor and fault plane solutions for a population of earthquakes. *Bulletin of the Seismological Society of America*, *80*, 600–614. https://doi.org/10.1785/BSSA0800030600

Ross, Z. E., & Cochran, E. S. (2021). Evidence for latent crustal fluid injection transients in Southern California from long-duration earthquake swarms. *Geophysical Research Letters*, *48*(12), e2021GL092465. https://doi.org/10.1029/2021GL092465

Roure, F., Brun, J.-P., Colletta, B., & Van Den Driessche, J. (1992). Geometry and kinematics of extensional structures in the Alpine foreland basin of Southeastern France. *Journal of Structural Geology*, *14*(5), 503–519. https://doi.org/10.1016/0191-8141(92)90153-N

Roure, F., Brun, J. P., Colletta, B., & Vially, R. (1994). Multiphase extensional structures, fault reactivation, and petroleum plays in the Alpine foreland basin of Southeastern France. In A. Mascle (Ed.), *Hydrocarbon and petroleum geology of France* (pp. 245–268). Springer Berlin Heidelberg. https://doi.org/10.1007/978-3-642-78849-918

Rutter, E. H., Holdsworth, R. E., & Knipe, R. J. (2001). The nature and tectonic significance of fault-zone weakening: An introduction. *Geological Society, London, Special Publications*, *186*(1), 1–11. https://doi.org/10.1144/GSL.SP.2001.186.01.01

Sebastiani, G., Govoni, A., & Pizzino, L. (2019). Aftershock patterns in recent central Apennines sequences. *Journal of Geophysical Research: Solid Earth*, *124*(4), 3881–3897. https://doi.org/10.1029/2018JB017144

Shelly, D. R. (2020). A high resolution seismic catalog for the initial 2019 Ridgecrest earthquake sequence: Foreshocks, aftershocks, and faulting complexity. *Seismological Research Letters*, *91*(4), 1971–1978. https://doi.org/10.1785/0220190309

Sibson, R. H. (1994). An assessment of field evidence for Byerlee friction. *Pure and Applied Geophysics*, *142*(3–4), 645–662. https://doi.org/10.1007/BF00876058

Sibson, R. H., & Xie, G. (1998). Dip range for intracontinental reverse fault ruptures: Truth not stranger than friction? *Bulletin of the Seismological Society of America*, *88*(4), 1014–1022. https://doi.org/10.1785/BSSA0880041014

Sirorattanakul, K., Ross, Z. E., Khoshmanesh, M., Cochran, E. S., Acosta, M., & Avouac, J.-P. (2022). The 2020 Westmorland, California earthquake swarm as aftershocks of a slow slip event sustained by fluid flow. *Journal of Geophysical Research: Solid Earth*, *127*(11), e2022JB024693. https://doi.org/10.1029/2022JB024693

Tesei, T., Collettini, C., Barchi, M. R., Carpenter, B. M., & Di Stefano, G. (2014). Heterogeneous strength and fault zone complexity of carbonate-bearing thrusts with possible implications for seismicity. *Earth and Planetary Science Letters*, *408*, 307–318. https://doi.org/10.1016/j.epsl.2014.10.021

Thomasset, C., Ritz, J. F., Pouliquen, S., Manchuel, K., & Le-Roux-Mallouf, R. (2024). Geometry and tectonic history of the north-eastern Cévennes faults system (SE Basin, France): New insights from deep seismic reflection profiles. *Bulletin de la Société Géologique de France – Earth Sciences Bulletin*, *195*, 17. https://doi.org/10.1051/bsgf/2024016

Thouvenot, F., Fréchet, J., Tapponnier, P., Thomas, J.-C., Le Brun, B., Ménard, G., et al. (1998). The M_L 5.3 Epagny (French Alps) earthquake of 1996 July 15: A long-awaited event on the Vuache Fault. *Geophysical Journal International*, *135*(3), 876–892. https://doi.org/10.1046/j.1365-246X.1998.00662.x

Thouvenot, F., Jenatton, L., & Gratier, J.-P. (2009). 200-m-deep earthquake swarm in Tricastin (lower Rhône Valley, France) accounts for noisy seismicity over past centuries. *Terra Nova*, *21*(3), 203–210. https://doi.org/10.1111/j.1365-3121.2009.00875.x

Truttmann, S., Diehl, T., & Herwegh, M. (2023). Hypocenter-based 3D imaging of active faults: Method and applications in the Southwestern Swiss Alps. *Journal of Geophysical Research: Solid Earth*, *128*(6), e2023JB026352. https://doi.org/10.1029/2023JB026352

Turner, J. P., & Williams, G. A. (2004). Sedimentary basin inversion and intra-plate shortening. *Earth-Science Reviews*, *65*(3), 277–304. https://doi.org/10.1016/j.earscirev.2003.10.002

Turrini, C., Angeloni, P., Lacombe, O., Ponton, M., & Roure, F. (2015). Three-dimensional seismo-tectonics in the Po Valley basin, Northern Italy. *Tectonophysics*, *661*, 156–179. https://doi.org/10.1016/j.tecto.2015.08.033

Utsu, T. (1961). A statistical study on the occurrence of aftershocks. *Geophysical Magazine*, *30*, 521–605.

Utsu, T., Ogata, Y., S, R., & Matsu'ura (1995). The centenary of the Omori formula for a decay law of aftershock activity. *Journal of Physics of the Earth*, *43*(1), 1–33. https://doi.org/10.4294/jpe1952.43.1

Vallage, A., Bollinger, L., Champenois, J., Duverger, C., Trilla, A. G., Hernandez, B., et al. (2021). Multitechnology characterization of an unusual surface rupturing intraplate earthquake: The ML 5.4 2019 Le Teil event in France. *Geophysical Journal International*, *226*(2), 803–813. https://doi.org/10.1093/gji/ggab136

Valoroso, L., Chiaraluce, L., & Collettini, C. (2014). Earthquakes and fault zone structure. *Geology*, *42*(4), 343–346. https://doi.org/10.1130/G35071.1

Valoroso, L., Chiaraluce, L., Piccinini, D., Di Stefano, R., Schaff, D., & Waldhauser, F. (2013). Radiography of anormal fault system by 64,000 high-precision earthquake locations: The 2009 L'Aquila (Central Italy) case study. *Journal of Geophysical Research: Solid Earth*, *118*(3), 1156–1176. https://doi.org/10.1002/jgrb.50130

Van den Ende, M., Ampuero, J.-P., Courboulex, F., Delouis, B., Godano, M., Larroque, C., & Sladen, A. (2024). Distributed acoustic sensing for aftershock monitoring: The case of the 2019 Mw 4.9 le Teil earthquake. *EarthArXiv preprint*. https://doi.org/10.31223/X5DX26

Volpe, G., Pozzi, G., Locchi, M. E., Tinti, E., Scuderi, M. M., Marone, C., & Collettini, C. (2023). Rheological heterogeneities at the roots of the seismogenic zone. *Geology*, *51*(10), 988–992. https://doi.org/10.1130/G51432.1

Waldhauser, F., & Ellsworth, W. L. (2000). A double-difference earthquake location algorithm: Method and application to the Northern Hayward Fault, California. *Bulletin of the Seismological Society of America*, *90*(6), 1353–1368. https://doi.org/10.1785/0120000006

Wetzler, N., Lay, T., Brodsky, E. E., & Kanamori, H. (2018). Systematic deficiency of aftershocks in areas of high coseismic slip for large subduction zone earthquakes. *Science Advances*, *4*(2), eaao3225. https://doi.org/10.1126/sciadv.aao3225

Woessner, J., Schorlemmer, D., Wiemer, S., & Mai, P. M. (2006). Spatial correlation of aftershock locations and on-fault main shock properties. *Journal of Geophysical Research*, *111*(B8), B08301. https://doi.org/10.1029/2005JB003961

Yamada, M., Kandel, T., Tamaribuchi, K., & Ghosh, A. (2019). 3D fault structure inferred from a refined aftershock catalog for the 2015 Gorkha earthquake in Nepal. *Bulletin of the Seismological Society of America*, *110*(1), 26–37. https://doi.org/10.1785/0120190075

Yukutake, Y., & Iio, Y. (2017). Why do aftershocks occur? Relationship between mainshock rupture and aftershock sequence based on highly resolved hypocenter and focal mechanism distributions. *Earth Planets and Space*, *69*, 1–15. https://doi.org/10.1186/s40623-017-0650-2

Yukutake, Y., Yoshida, K., & Honda, R. (2022). Interaction between aseismic slip and fluid invasion in earthquake swarms revealed by dense geodetic and seismic observations. *Journal of Geophysical Research: Solid Earth*, *127*(4), e2021JB022933. https://doi.org/10.1029/2021JB022933